Received: 24 July 2020 | Revised: 16 April 2021 | Accepted: 19 April 2021

DOI: 10.1002/esp.5142

RESEARCH ARTICLE

ESPL WILEY

From consumer to enterprise grade: How the choice of four UAS impacts point cloud quality

Manuel Stark[1] | Tobias Heckmann[1] | Livia Piermattei[2] | Fabian Dremel[1] | Andreas Kaiser[3] | Patrick Machowski[4] | Florian Haas[1] | Michael Becht[1]

[1]Department of Physical Geography, Catholic University Eichstaett-Ingolstadt, Eichstaett, 85072, Germany

[2]Department of Geosciences, University of Oslo, Oslo, 0316, Norway

[3]Climate Protection Management, District Administration Siegen-Wittgenstein, Siegen, 57072, Germany

[4]Quantum Systems, Gilching, 82205, Germany

Correspondence
Manuel Stark, Department of Physical Geography, Catholic University Eichstaett-Ingolstadt, Eichstaett 85072, Germany.
Email: mstark@ku.de

Abstract

Uncrewed aerial systems (UAS), combined with structure-from-motion photogrammetry, has already proven to be very powerful for a wide range of geoscience applications and different types of UAS are used for scientific and commercial purposes. However, the impact of the UAS used on the accuracy of the point clouds derived is not fully understood, especially for the quantitative analysis of geomorphic changes in complex terrain. Therefore, in this study, we aim to quantify the magnitude of systematic and random error in digital elevation models derived from four commonly used UAS (XR6/Sony α6000, Inspire 2/X4s, Phantom 4 Pro+, Mavic Pro) following different flight patterns. The vertical error of each elevation model is evaluated through comparison with 156 GNSS reference points and the normal distribution and spatial correlation of errors are analysed. Differences in mean errors (−0.4 to −1.8 cm) for the XR6, Inspire 2 and Phantom 4 Pro are significant but not relevant for most geomorphological applications. The Mavic Pro shows lower accuracies with mean errors up to 4.3 cm, thus showing a higher influence of random errors. QQ plots revealed a deviation of errors from a normal distribution in almost all data. All UAS data except Mavic Pro exhibit a pure nugget semivariogram, suggesting spatially uncorrelated errors. Compared to the other UAS, the Mavic Pro data show trends (i.e. differences increase with distance across the survey—doming) and the range of semivariances is 10 times greater. The lower accuracy of Mavic Pro can be attributed to the lower GSD at the same flight altitude and most likely, the rolling shutter sensor has an effect on the accuracy of the camera calibration. Overall, our study shows that accuracies depend highly on the chosen data sampling strategy and that the survey design used here is not suitable for calibrating all types of UAS camera equally.

KEYWORDS
error comparison, spatial autocorrelation, structure-from-motion photogrammetry, topographic surveying, uncrewed aerial system, unmanned aerial systems

1 | INTRODUCTION

The combination of uncrewed aerial systems (UAS) image data with structure-from-motion (SfM) photogrammetry and multi-view-stereo (MVS) workflows is regarded as a powerful tool for precise surface reconstructions in a wide range of geosciences (e.g. Carrivick et al., 2016; Eltner et al., 2016; Harwin & Lucieer, 2012; James et al., 2017a) such as glaciology (e.g. Piermattei et al., 2016; Rossini et al., 2018), soil science (e.g. Krenz et al., 2019), forestry (e.g. Zhang et al., 2019) or geomorphology (e.g. Hamshaw et al., 2019; Koci et al., 2017). UAS imagery combined with SfM-MVS allows 3D point clouds to be obtained, from which it is possible to generate digital

elevation models (DEMs) of varying resolution, depending on the achieved ground sample distances (GSDs). Multi-temporal UAS-DEMs are often used to quantify surface elevation changes with reported magnitudes of change between a few centimetres and several metres (e.g. Neugirg et al., 2016; Stark et al., 2020). Often, those studies have been carried out in challenging environments (e.g. Gindraux et al., 2017; Neugirg et al., 2016) characterized by demanding operating factors such as insufficient positioning signal and a complex morphology with an increased risk of crashing. Therefore, the choice of appropriate UAS is a trade-off between price, system performance (size, weight, motor speed, platform design, etc.), specific site conditions and the accuracies required for the research topic. Generally, the principle of 'as accurate as required but also as efficient as possible' should be applied. In the last decade, the fast and steady development in the UAS sector brought a wide range of remotely controlled aerial vehicles of different types (fixed-wing, multi-rotor), prices and dimensions to the consumer market (Colomina & Molina, 2014). The mounted cameras (e.g. RGB, thermal, multispectral) and sensor designs (global shutter, rolling shutter) vary widely and so do the corresponding image resolutions. Considering the myriad of potential combinations of system and sensors, we see the necessity to investigate in the quality of UAS-DEMs further. Therefore, we analysed the vertical accuracy and error distribution of various DEMs obtained by four flight systems commonly used in geomorphic research. Since there is no official price classification of UAS in terms of which system can be attributed to 'consumer grade' and which to 'high end' (professional to enterprise grade), we have set a price threshold of €2000 for 'consumer-grade' UAS.

Data generated from modern topographic techniques are affected by random and systematic errors (Milan et al., 2011). Commonly, the accuracy of the DEM is evaluated against reference data with higher known accuracy. Statistical parameters of accuracy and precision such as mean, standard deviation and root mean square error (RMSE) are then calculated. The mean is an indicator of systematic error, but it does not identify the spatial distribution of errors. Similarly, RMSE or robust statistics such as the normalized median absolute deviation (Hoaglin et al., 1983, cited in Höhle & Höhle, 2009) are not sufficient to detect systematic errors, which is crucial in quantitative geomorphological analyses. DEM errors can be introduced by numerous factors, such as (i) survey point quality, (ii) data sampling strategy (Gindraux et al., 2017) or (iii) topographic complexity (Kraus et al., 2006; Milan et al., 2011; Müller et al., 2014). Factors (i) and (ii) are mainly a function of sensor quality and survey design (Carbonneau & Dietrich, 2017) while factor (iii) is defined by the morphology and surface characteristics of the respective study site. Concerning sensor quality, rolling shutter cameras can be modelled less effectively than those with global shutters (Vautherin et al., 2016) when applying photogrammetric procedures. Another source of error is the inaccurate modelling of lens parameters in photogrammetric software products, which can result from on-board image preprocessing (James et al., 2020). Different lens models will require different qualities of image network to determine their parameter values accurately (Fraser, 2001; Gruen & Beyer, 2001).

Based on these previous studies, we saw the need to further investigate the degree of error in UAS-derived photogrammetric DEMs. Specifically, we consider four different UAS to address the following four objectives. (1) Defining the influence of sensors and flight patterns and (2) exploring the influence of terrain factors on DEM accuracy. Since a higher spatial correlation of errors tends to have a larger impact on the total uncertainty budget (Anderson, 2019) of a DEM-of-difference (DoD), we further investigate (3) the spatial pattern and magnitude of differences in several DoDs when UAS are changed between acquisitions (under stable environmental conditions). With objective (3) we mainly aim to increase our understanding of systematic errors in a given DoD, because systematic errors can fundamentally

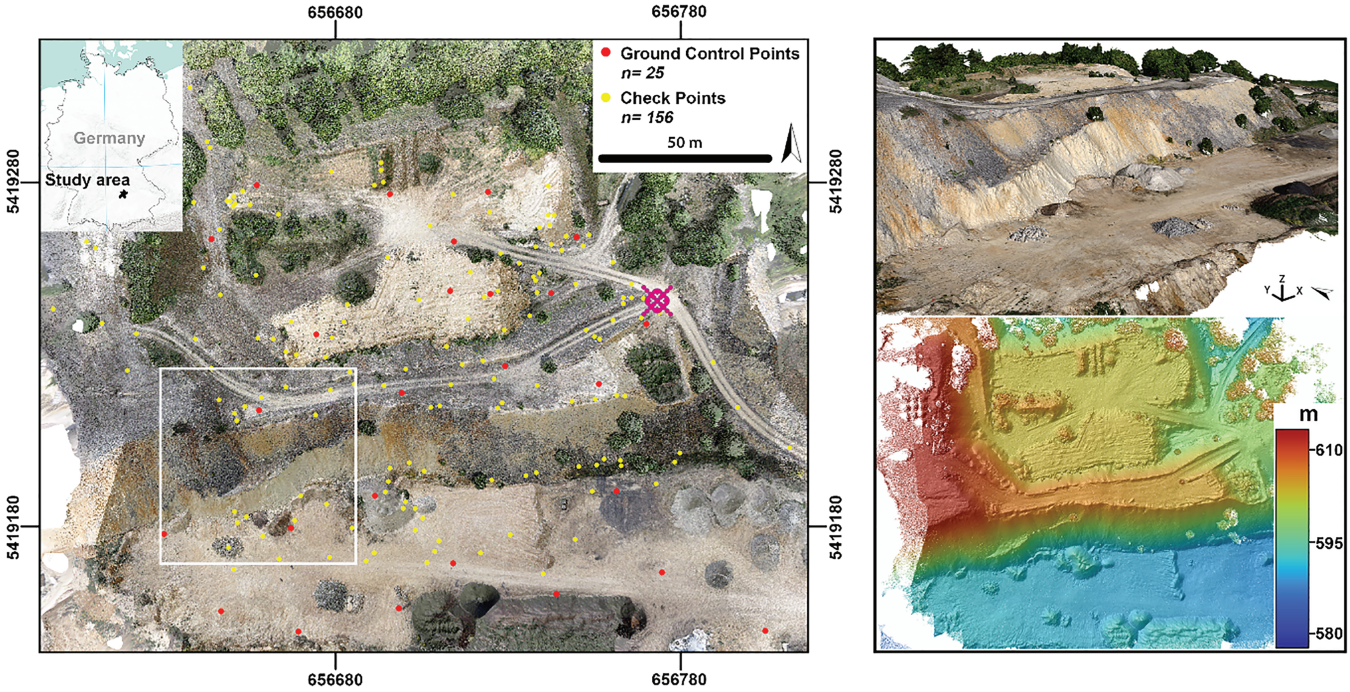

FIGURE 1 Research site (left) with 3D oblique view (top right) and DEM (bottom right). The white square in the research site marks the subset for the experimental multi-temporal (DoD) approach. The purple symbol in the left figure marks the UAS launch point [Color figure can be viewed at wileyonlinelibrary.com]

affect the way topography is represented in a DEM (Kasprzak et al., 2018) and characterize the correlation structure of random errors (Anderson, 2019). Several studies have examined the accuracy of photogrammetric UAS data with relation to ground control point (GCP) distribution (Gindraux et al., 2017; James et al., 2017b), flight design (Gerke & Przybilla, 2016; Sanz-Ablanedo et al., 2020), image overlaps (Torres-Sánchez et al., 2018), GSDs and camera systems (e.g. Mosbrucker et al., 2017) and processing parameters (Gindraux et al., 2017; James et al., 2017a). However, it is still unclear to which degree DEMs obtained by UAS of varying prices are affected by random and systematic errors. Many of the previously mentioned studies have been carried out with consumer-grade UAS. This is understandable, since from a global perspective, 'high-end' UAS and the necessity of additional operational training may be unaffordable for a large number of (research) institutes. Therefore, we further (4) evaluate whether a specific flight pattern (carried out at a constant flight height) and post-processing of 'consumer-grade' UAS data can generate results comparable to so-called 'high-end' UAS, by discussing the implications of our findings for geomorphological applications. In order to assess the cause of error in photogrammetric DEMs from four different UAS, we carried out a careful inspection of the bundle adjustment (BA) results before evaluating and comparing the respective errors.

2 | MATERIALS AND METHODS

2.1 | Study area

The study site (656 703 E; 5 419 175 N/UTM32N; European Petroleum Survey Group Geodesy code 25832) (Figure 1) is part of a limestone quarry located 3.5 km northwest of the city of Eichstaett, Germany and spans a shape area of approximately 37 000 m^2 with elevations ranging from 582 to 617 m (ETRS 89). The quarry is mainly formed by dumped limestone plates and gravel, deposited sands, soils and granite bricks of approximate 0.1 m edge length, sparse vegetation and dirt tracks. We choose the study site because of its complex terrain, with a wide variety of surface covers, roughness and landforms, which allow us to investigate the impact of certain terrain factors (Gerke & Przybilla, 2016) on DEM accuracy. Terrain compositions can have a direct impact on UAS surveys (Gerke & Przybilla, 2016). Elevation changes, for example, can cause varying image overlaps when operating at a constant altitude above launch point, as in the present study.

FIGURE 2 Tested UAS: Mavic Pro, Phantom 4 Pro+, Inspire 2 and XR6 (from left to right) [Color figure can be viewed at wileyonlinelibrary.com]

2.2 | UAS and flight pattern

We tested three standard and one customized multi-rotor UAS of different sizes and prices (Figure 2 and Table 1). The Mavic Pro, Phantom 4 Pro+ and Inspire 2/X4s are off-the-shelf systems manufactured by Da-Jiang Innovations Science & Technology Co., Ltd (DJI). The XR6 was developed by Airborne Robotics & geo-konzept GmbH and is fully assembled with a Sony α6000 system camera with a fixed wide-angle Sigma lens.

Three different flight patterns (Figure 3) were carried out for each UAS. The UAS headings are east for parallel axes (PA) flights, north for cross-grid (CG) flights and towards the centre of the area of interest for cross-grid-circle (CGC) flights. The point of interest (PoI) flight is composed of off-nadir images with a camera tilt of 35°, as suggested by Nesbit and Hugenholtz (2019), and with the camera always pointing towards the centre of the study site. The information required for each flight path commonly includes the global position of each waypoint, the flying height, the speed and heading of the UAS as it approaches the waypoint and the image overlap (Table 2). For the Phantom 4 Pro+, the flight information is set manually during the flight so we deploy a pre-defined camera trigger every 2 s with an airspeed of 3 m/s to guarantee an overlap, comparable to the other systems. Since not all UAS support the same flight planning software, we use two different software

TABLE 1 Manufacturers' information on the tested UAS (CMOS = complementary metal–oxide–semiconductor)

UAS	Mavic pro	Phantom 4 pro	Inspire 2	XR6
Manufacturer	DJI	DJI	DJI	Airborne Robotics & geo-konzept GmbH
Camera	Internal device	Internal device	Zenmuse X4s	Sony α6000
Focal length [mm]	26	24	24	28.5
Sensor	Sony 1/2.3" CMOS	Sony 1" CMOS	Sony 1" CMOS	Sony EXMOR APS HD CMOS
Sensor resolution [pixels]	4096 × 2160	5472 × 3648	5472 × 3648	6058 × 4012
Pixel pitch [μm]	1.51	2.41	2.41	3.88
Take-off weight [g]	734	1388	3440	4990
Rotor count	4	4	4	6
Size (diameter in cm)	33.5	35	85	95
Application flight time [min]	27	30	27	20
Range [km]	7	7	7	1.5
Critical wind velocity [kmf/h]	>36	>36	>36	>36
Price [€]	999	1996	3399	25 300

products for our study. The XR6 flights were configured with Mission Planner (freeware by Ardupilot, Version 1.3.52), while the flight configurations for Mavic Pro and Inspire 2 were designed with DJI Ground Station Pro. Flights were taken between 11:00 and 14:30 UTC under stable weather conditions (sunny, no clouds) with a steady wind velocity of 12 km/h (approximately 6.5 knots) from the southeast. For efficiency reasons, we choose to store the images directly in JPG format. Image overlaps were chosen to gain high redundancy in image content in order to minimize systematic errors in UAS surveys (Luhmann et al., 2016). Aperture settings, focus, white balance and ISO were defined automatically but kept stable for each survey.

The rationale for flying all systems at the same height irrespective of the expected GSDs was justified by the possibility of directly comparing results from a flight height commonly used in geoscience (see Table A1 in the Appendix). Achieving a consistent GSD for all systems would have resulted in a much slower survey, lower flight height and higher number of images for the Mavic Pro system. Due to efficiency reasons in terms of both data acquisition and processing effort (data size, CPU performance, RAM, etc.), we refrained from flying the UAS below 80 m. Another reason for the chosen flight height was compliance with the German national regulation on UAS operations (German Federal Ministry of Transport and Digital Infrastructure, 2020). This limits flight height to within 100 m above the ground, while keeping a safe distance from critical infrastructure such as power lines (in Germany, these are commonly between 30 and 60 m high) (Federal Network Agency of Germany, 2019). Note that the terrain varies from approximately 580 to 615 m in elevation, while the UAS launch point is at 600 m, which implies effective flight heights between 65 and 100 m above ground.

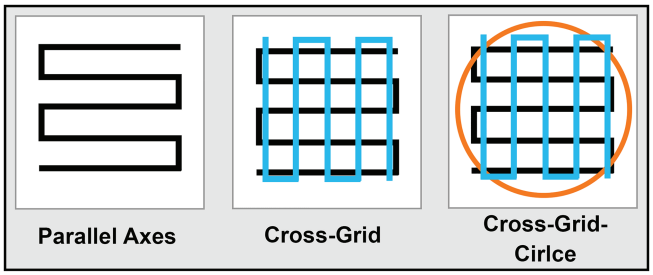

FIGURE 3 Flight patterns. The orange circle shows the flight path for the convergent images while the black and blue lines show the structure of the parallel-axes flights [Color figure can be viewed at wileyonlinelibrary.com]

2.3 | Global navigation satellite systems data

GCPs were designed as red carpets (40 × 40 cm). A reflector (10 cm diameter) was placed in the centre of each carpet and stones were placed at every corner to prevent movement by wind. 25 GCPs were spread and served for a global exterior orientation. We aimed for a GCP spacing of 15–80 m (Gindraux et al., 2017; James et al., 2017a) and a uniform distribution (horizontally and in elevation) of GCPs across the study site. Additionally, we collected 156 independent check points (CPs) on natural surfaces, which serve as reference data for addressing vertical differences between DEMs and CPs (James & Robson, 2014; James et al., 2017a). CPs were distributed randomly, covering the entire area of interest to allow for a differentiated analysis of vertical offsets between CPs and 3D points. All points were measured with a Stonex S9III global navigation satellite system (GNSS) in real-time kinematic mode, controlled by a Nomad handheld computer (Windows mobile 6.1). Mean standard deviations (StDs) of GNSS data are given in Table 3 (a complete list of all GCP and CP StDs is given in Table A2 in the Appendix).

2.4 | Data processing of UAS imagery

We implemented a standard SfM-MVS workflow (Figure 4) in Photoscan Pro by Agisoft LLC (Version 1.4.2) to process the UAS images into 3D point clouds (autocalibration of lens parameters). Lane et al. (2004) have shown that random errors in exterior orientation parameters can propagate into systematic DEM errors. Therefore, we eliminated five error-prone GCPs due to insufficient positioning signal in certain parts of the area of interest. BA parameters have been chosen following James et al. (2017a) but including two affine distortion coefficients (b_1 and b_2). Computer specifications are as follows: DELL Precision 7510 with 32GB RAM, Nvidia Quadro M2000 graphic card and Intel i7 processor.

TABLE 3 Mean accuracies of GNSS coordinate measures. Note that the distance to the closest SAPOS station (providing a correction signal for real-time kinematic [RTK] measures) is less than 10 km; coordinates (European Petroleum Survey Group Geodesy code 25832) 657 512.393, 5 418 703.245, 583.25 m

Direction	StD [m]
X-coordinate	0.007
Y-coordinate	0.004
Z-coordinate	0.012

TABLE 2 UAS survey parameters for all flights

					Survey time [min]			Image count		
UAS type	ISO	UAS altitude [m]	Air speed [m/s]	Overlap (front & side) [%]	PA	CG	CGC	PA	CG	CGC
Mavic Pro	100	80	5	80/75%	3:00	4:00	3:40	48	70	41
Phantom 4 Pro+	100	80	app. 4	app. 80/75%	3:20	3:29	2:54	38	48	30
Inspire 2	400	80	7.8	80/75%	1:32	2:30	2:28	33	50	36
XR6	250	80	5	80/75%	3:11	3:10	3:00	50	60	18

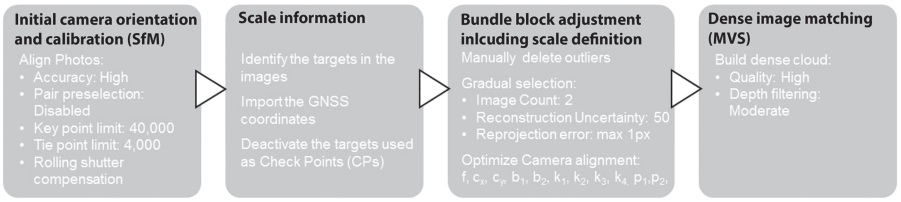

FIGURE 4 Workflow and parameters used for point cloud generation with Agisoft PhotoScan Pro

TABLE 4 SfM point cloud densities (mean value)

	Point density [points*m^{-1}]		
UAS	PA	CG	CGC
Mavic Pro	386	444	387
Phantom 4 Pro+	617	623	517
Inspire 2	595	681	544
XR6	1020	1240	1030

2.5 | Data analysis

2.5.1 | DEM generation and assessment of vertical DEM errors (random and systematic)

To address the differences between the point clouds and CPs, we calculated local meshes by 2D Delaunay triangulations in SAGA LIS/GIS for all point clouds. The meshes are computed within a predefined 2D neighbourhood search radius of 1 m around every CP (point cloud densities 386 to 1240 p/m^2; Table 4). The elevation differences between the respective CPs and the local meshes are calculated along the plumbs of the respective CPs and expressed as error statistics. We chose the point-to-mesh-distance approach to avoid incorrect estimates of elevation differences caused by short horizontal offsets between the reference and UAS data in point-to-point measurements, especially in areas of steep slopes and sudden terrain changes (Müller et al., 2014). Formulas to describe the accuracy of a DEM based on the RMSE, mean error, absolute mean error or StD can be found, for example, in Höhle and Höhle (2009) but those descriptors are only appropriate with normally distributed random errors. As outliers can negatively affect both error statistics and distribution, we filtered all CPs with differences larger than three times the respective StD. Generally, the accuracy of a photogrammetric-derived DEM is highly subject to spatially non-independent (systematic) errors (Lane et al., 2003).

To describe the systematic error in each dataset, we applied a two-sided *t*-test with $\alpha = 0.05$ to the differences. Given the large sample size ($n = 156$) and, consequently, the enhanced tendency to reject the null hypothesis, we additionally evaluated the effect size after Cohen. Komolgorov–Smirnov tests with Lilliefors correction (R package *nortest*; Gross & Ligges, 2015) were used to test whether the differences for each UAS/flight pattern follow a normal distribution. In the next step, we calculated semivariograms of all data (differences) to explore the degree and range of spatial autocorrelation.

2.5.2 | Correlation analysis of terrain factors

In order to explore the dependence of error on topography, we computed Spearman rank correlations between measured differences and selected terrain factors. Slope (Zevenbergen & Thorne, 1987), roughness (StD of slope) and general curvature (Zevenbergen & Thorne, 1987) were derived from a DEM005 that was smoothed using a moving window mean filter with radius $r = 5$ cells. This filter radius was found to yield the highest correlations with the CP differences in a series of tests covering radii between 1 and 10 cells. Both signed and unsigned differences were analysed for correlation with terrain factors using the Spearman rank correlation coefficient. We did this because we assumed that some terrain factors would be related more to the magnitude than to the direction of differences (e.g. roughness or slope; see Scheidl et al., 2008), which would be reflected in a correlation with unsigned differences. In contrast, other terrain properties could lead to a more systematic difference (e.g. curvature), which would be indicated by a correlation with signed differences.

2.5.3 | Creation of DEM of differences

For a more geomorphological perspective on the resulting uncertainties, we also investigated error assessments based on multi-temporal DEM analysis. As topographic changes certainly did not occur between flights, the resulting DoD represents 'stable areas' throughout the whole area and can be used to investigate (i) the effect of using different UAS (CG pattern) in multi-temporal surveys and (ii) the influence of various terrain factors with a very large number of observations.

In reality, even in carefully designed and processed surveys, small systematic (and random) errors will remain in data (Sanz-Ablanedo et al., 2020) and may be further reduced by co-registration procedures (Anderson, 2019). So, we applied iterative closest point (ICP) algorithms in the SAGA-LIS software to all point clouds with the XR6 CG dataset as reference. DoDs were calculated before and after ICP adjustments. To arrive at a more robust adjustment, we used pre-computed normal vectors (for each point) so that only areas with similar orientation are considered for the error minimization (Besl & McKay, 1992). The maximum nearest neighbour distance for two points to be considered as homologous was at 0.2 m for all adjustments. After co-registration, the point clouds were rasterized with a bilinear resampling scheme to a 0.05 m cell-sized DEM of common extent. If multiple points correspond to one grid cell, the mean *z*-value of the respective points was used for aggregation.

Even though ICP adjustments can minimize systematic errors (James & Robson, 2014), it will not be possible to reduce them to zero. To evaluate the effect of co-registration on systematic errors and to provide an estimate of the remaining error in co-registered DoDs, we also calculated the semivariances of DoDs before and after ICP adjustments. The semivariogram range of a DoD

functions as a measure of space in which DoD errors are correlated and can be used for error propagation methods (e.g. the concept of spatially variable errors and levels of detection [LoD]; Wheaton et al., 2010). Error descriptors that relate to the precision of individual measurements (e.g. StD) only, or metrics that involve absolute values or square of individual records (e.g. RMSE), tend to have little impact on the accuracy of a volumetric change estimate and should not be seen as a representative of DoD quality (Anderson, 2019). Figure 5 summarizes the entire workflow of data surveying, processing and analysis.

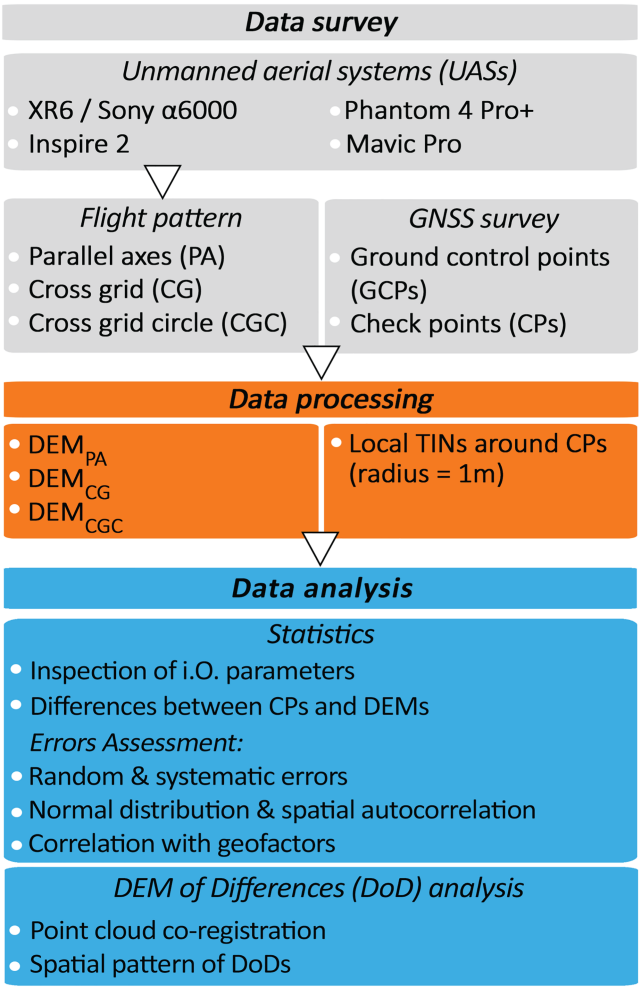

FIGURE 5 Workflow of data surveying, processing and analyses [Color figure can be viewed at wileyonlinelibrary.com]

3 | RESULTS AND DISCUSSION

3.1 | SfM-MVS results

3.1.1 | Point cloud generation and uncertainty estimation of camera parameters

Image alignment was successful for all data. Processing time was between 13 min (Mavic Pro, PA data) and 6 h 15 min (XR6, CGC data). The overall tie-point count ranged from 32 583 (Mavic Pro, PA) to 311 699 points (Inspire 2, CGC) (Table 4). GSD varies from 1.4 cm (XR6, CG) to 2.5 cm (Mavic Pro, PA) (Table 5). Figure 6 shows an example of tie-point density and distribution across the different data. The RMSE on GCPs for surveys with the XR6 and the Inspire 2 can be regarded as equal, whereas the Phantom 4 Pro+ data are weaker by a factor of two in all flight patterns (Table 5). This is interesting because the Inspire 2 and Phantom 4 Pro+ are equipped with the same sensor and, apart from the manual control of the Phantom 4 Pro+, all flight parameters were kept stable for the entire survey. It is possible that the differences may be due to different in-camera processors (RAW to JPG conversion), but testing this would require further investigations. It is more likely that variable image overlaps cause the high errors in external orientation of the Phantom 4 Pro+ data. This assumption is supported by the higher RMSE on GCPs of the Phantom 4 Pro+ data when compared to the Inspire 2 data (Table 5). The Mavic Pro data stand out as the RMSE surpasses the error of the Phantom 4 Pro+ data by a factor of two and by a factor of four when compared to Inspire 2 and XR6 data. The RMSEs of GCPs of the XR6, Inspire 2 and Phantom 4 Pro+ data are consistent across all flight patterns. This is not the case for the Mavic Pro system, where the CG dataset shows lower errors than data obtained by PA and CGC flights.

The strong systematics in Figure A1 in the Appendix suggest that the weak modelling of lens distortion is likely to be responsible for the large error in units of pixel dimensions (2.8) in the Mavic Pro data (all other UAS ≤ 0.5) (Table 5). Moreover, the sensor of the Mavic Pro yielded a larger GSD when compared to the other systems, and a low pixel count corresponding to the GCP reflectors (Figure 7) makes an accurate GCP marker placement in Mavic Pro images difficult. As Mosbrucker et al. (2017) revealed that GSD is the most influential factor when predicting point cloud quality (accuracy), we assume that the results could be improved if surveys were acquired with a smaller GSD. Nevertheless, despite the almost similar GSD of the Inspire 2 and Phantom 4 Pro+ data, the RMSE of GCPs [cm] of the Phantom 4 Pro clearly exceeds the error of the Inspire 2 by an order of two

TABLE 5 Ground sample distances for images (mean value) and digital orthomosaics (DOM); used tie points and GCP RMSE, by flight pattern

	GSD [cm]				Used tie points			GCP RMSE [cm] (pixel)		
		Orthomosaic								
UAS	Single nadir image	PA	CG	CGC	PA	CG	CGC	PA	CG	CGC
Mavic Pro	2.27	2.54	2.37	2.54	32 583	72 453	104 760	24 (2.4)	15 (2.8)	11 (1.1)
Phantom 4 Pro+	1.87	1.99	2.00	2.20	38 719	45 764	55 390	9.9 (0.3)	10 (0.2)	10 (0.4)
Inspire 2	1.91	2.05	1.92	2.14	40 220	102 091	311 699	5.3 (0.3)	5.3 (0.4)	5.4 (0.4)
XR6	1.33	1.56	1.42	1.56	79 265	149 185	156 475	5.5 (0.3)	5.3 (0.5)	5.5 (0.4)

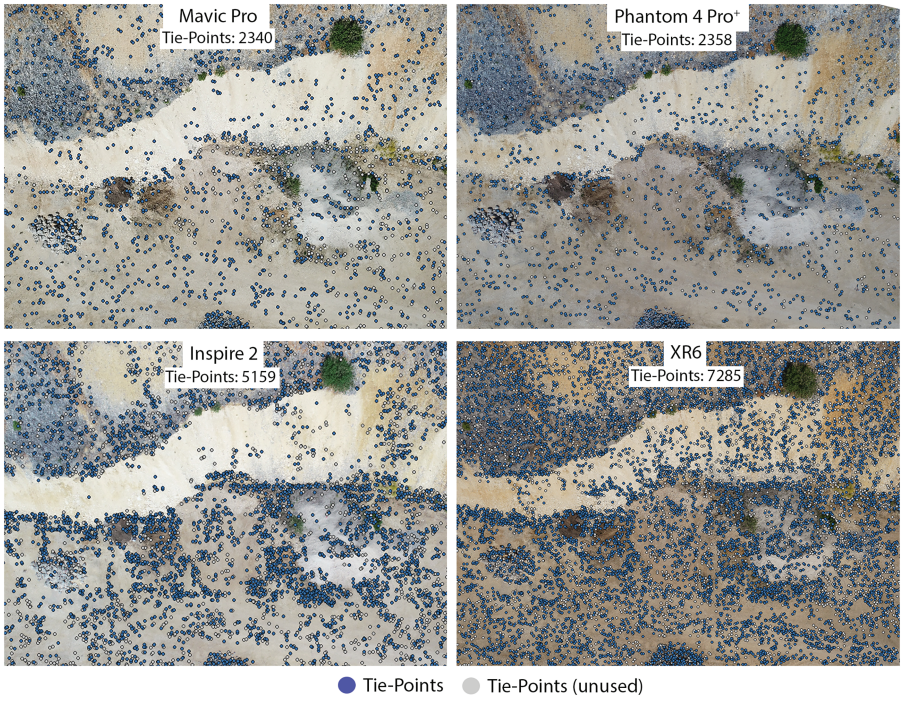

FIGURE 6 Tie points extracted from example images from different UAS (CG flight mode) [Color figure can be viewed at wileyonlinelibrary.com]

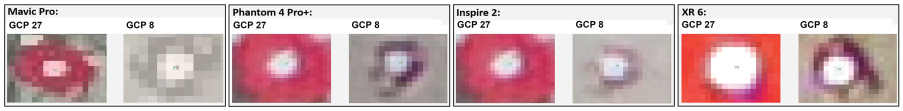

FIGURE 7 Different image resolution covering selected GCPs in the UAS datasets. Ground-sensor distances are 50 m (GCP 27) and 80 m (CGP 8) [Color figure can be viewed at wileyonlinelibrary.com]

(Table 5). We conclude that differences in RMSE of GCPs [cm] are caused by poorer estimation of exterior but also interior orientation parameters.

A large sensor also enables a wider ISO range and the camera can shoot at higher ISO speeds with a high signal-to-noise ratio. The low resolution and relatively small sensor of the Mavic Pro UAS enables an ISO range of 100–1600 only. This is quite low compared to the range of the Phantom 4 Pro+ and Inspire 2 (100–12 800) and the XR 6 system (10–25 600). Note that UAS surveys should be done at the lowest possible ISO value given the required shutter speed and aperture. Generally, ISO values above 400 should be avoided to maintain high-quality imagery.

3.1.2 | Autocalibration and variation of internal orientation parameters

Except for the XR6 data, all cameras show systematic residuals of more than 1 pixel after autocalibration (see Figure A1 in the Appendix). The same effect was observed by Przybilla et al. (2020), who assume that residuals are caused by aspherical lenses (P4P and Inspire 2) and rolling shutter effects (Mavic Pro). As a general result, K_i and P_i parameters show the lowest variations. All other internal orientation parameters show higher variations, especially those of the Mavic Pro system (Table 6). Variations in focal length estimates for the XR6 and the Inspire 2 can be regarded as equal, whereas the P4P system shows slightly higher variations. B_i parameters of the XR6 show a slightly higher variation than those of the Inspire 2 and Phantom 4 Pro+ datasets, pointing towards a greater influence of flight pattern on autocalibration. The largest variations can be found in Y_p and X_p.

High residuals in the distortion models of the Mavic Pro data suggest that the survey error is likely to be caused by a distortion model being poorly suited to the distortion pattern of the imagery. We assume that some imagery is likely to have undergone a higher degree of image on-board pre-processing, from raw DNG to JPG, than others. In such cases, distortion models will represent corrections to the initially applied manufacturer's corrections, which generally aim to reduce radial distortion while altering the relative importance of decentring distortions since the centre of the practical radial distortion may not be consistent with the centre of image format (James et al., 2020). Accuracy issues may also result from relatively weak image network geometry of the double grid, and of course parallel-axes flight plans, a configuration which has become standard in flight planning for topographic surveying (James et al., 2020).

3.1.3 | Correlation between internal orientation parameters

High correlations between internal orientation parameters can be a result of specific terrain morphology but also of data sampling strategy. As the study was carried out under stable environmental conditions, we assume that differences in correlations of internal orientation parameters result only from different flight patterns. In general, we observed only moderate correlations of internal orientation parameters with focal length, mainly Y_p and k_i (see Tables A3–A14 in the Appendix). The relationship is more pronounced in CGC datasets, especially in those obtained with the Phantom 4 Pro+ and Mavic Pro (Figure 8). The highest correlations can be found between focal length and Y_p and between X_p and p_1. X_p correlates with b_1 with

TABLE 6 Internal orientation parameters (f = focal length [principal distance], X_p = principal point offset of X-coordinate, Y_p = principal point offset of Y-coordinate, K_i = radial distortion coefficients, P_i = decentring distortion coefficients, b_i = affinity and orthogonality) and resulting StD with respect to all datasets

UAS	Flight pattern	F (pix)	X_p (pix)	Y_p (pix)	B_1	B_2	K_1	K_2	K_3	K_4	P_1	P_2
XR6/α6000	PA	4867.940	4.248	32.160	−3.396	−1.802	−0.110	0.180	−0.174	0.110	0.047	0.000
	CG	4872.170	−5.949	15.353	−0.482	0.305	−0.111	0.186	−0.183	0.111	0.000	0.000
	CGC	4865.910	−3.742	14.340	−0.522	0.211	−0.113	0.197	−0.215	0.143	0.000	−0.000
StD		*2.608*	*4.380*	*8.172*	*1.364*	*0.972*	*0.001*	*0.007*	*0.018*	*0.015*	*0.022*	*0.000*
Inspire 2/X4s	PA	3651.540	7.011	40.352	2.275	1.096	0.016	−0.090	0.181	−0.120	0.001	0.000
	CG	3654.15	3.206	29.443	0.483	0.721	0.013	−0.067	0.129	−0.080	0.001	0.000
	CGC	3657.74	3.284	29.199	0.386	0.679	0.012	−0.066	0.126	−0.078	0.001	0.000
StD		*2.542*	*1.776*	*5.201*	*0.869*	*0.186*	*0.002*	*0.011*	*0.025*	*0.019*	*0.000*	*0.000*
Phantom 4 Pro+	PA	3679.90	11.014	16.792	−8.883	−1.369	0.017	−0.069	0.133	−0.084	0.003	0.001
	CG	3677.40	26.535	23.260	−7.270	−0.003	0.018	−0.073	0.141	−0.090	0.003	0.001
	CGC	3685.00	28.309	25.050	−6.726	0.042	0.019	−0.076	0.146	−0.093	0.003	0.001
StD		*3.163*	*7.769*	*3.547*	*0.916*	*0.655*	*0.001*	*0.003*	*0.005*	*0.004*	*0.000*	*0.000*
Mavic Pro	PA	3026.81	−0.836	−131.219	−7.608	−13.037	0.079	−0.334	0.670	−0.462	0.001	0.001
	CG	3080.47	17.085	22.403	0.778	−0.021	0.120	−0.640	1.473	−1.160	0.000	0.001
	CGC	3109.04	9.765	−17.998	−5.050	3.417	0.130	−0.714	1.679	−1.356	−0.000	0.001
StD		*34.087*	*7.357*	*65.022*	*3.509*	*7.087*	*0.022*	*0.165*	*0.435*	*0.384*	*0.001*	*0.000*

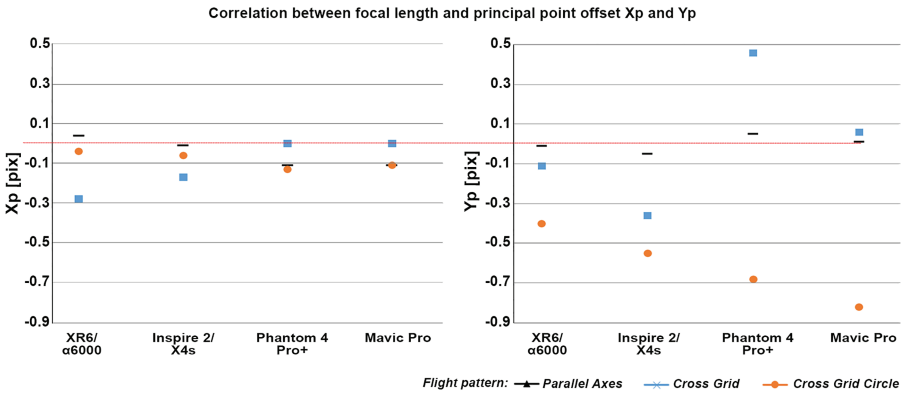

FIGURE 8 Correlation between f and X_p (left) and Y_p (right) with respect to all data [Color figure can be viewed at wileyonlinelibrary.com]

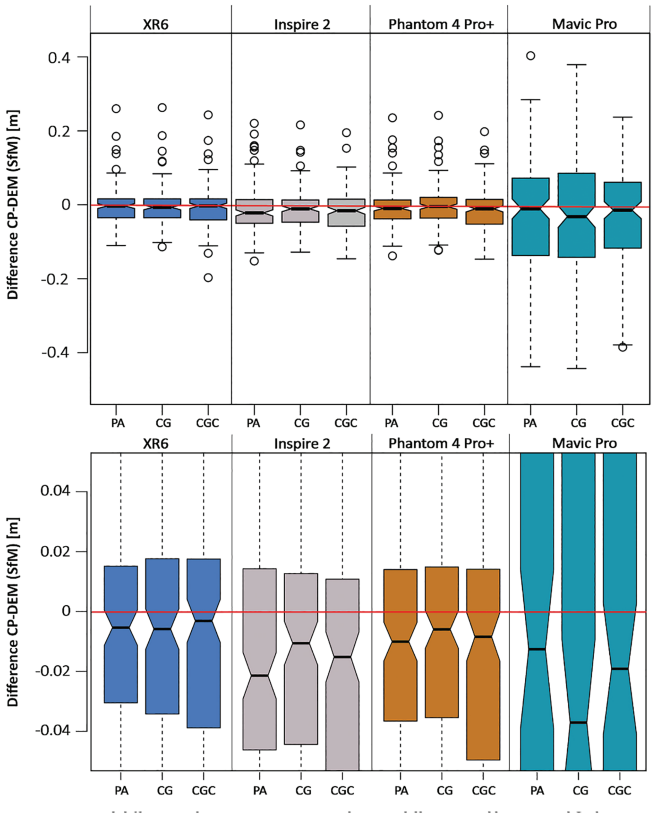

FIGURE 9 Vertical differences between GNSS-CPs and DEMs, differentiated by UAS and flight pattern (upper figure: limit of y-axis = 0.5; lower figure: limit of y-axis = 0.05) [Color figure can be viewed at wileyonlinelibrary.com]

the exception of the XR6 CG, CGC and all Inspire 2 datasets. As expected, k_i and p_i are internally correlated in all datasets, regardless of flight pattern or UAS.

Distortion parameter correlations for the Inspire 2 PA and CG data are comparable to those of the XR6 system, whereas the CGC dataset of the Inspire 2 system reports slightly stronger correlations between p_i and k_i. Interestingly, the PA datasets obtained with the Phantom 4 Pro+ and Mavic Pro system showed much stronger relationships between the X_p and Y_p and b_1 and b_2 than all other datasets, which again we assume to be caused by the factors (i) aspherical lens (Phantom 4 Pro+) and (ii) rolling shutter effects (Mavic Pro). Zhou et al. (2020) have shown that, especially in parallel-axes surveys, the correction of rolling shutter effect (as done in this study) improves results when processed with an eight-parameter optimization but that the best results are obtained by employing a 10-parameter camera model without rolling shutter compensation.

3.2 | Statistical properties

3.2.1 | Differences and random errors

The calculation of CP-DEM difference yielded different magnitudes but identical directions of errors for all data (Figure 9). Boxplots show that most distributions correspond to a slight overestimation of *z*-values in all data. Average differences (Table 7) are remarkably similar for all flight patterns of the UAS and there are no significant differences (overlapping notches) between the medians produced by different devices. Also, the spread of most distributions is remarkably similar, except for the Mavic Pro data. A Levene test suggests that the variances of XR6, Inspire 2 and Phantom 4 Pro+ can be considered equal ($p = 0.23$). The StD can be regarded as a measure of random error, so our data show that this uncertainty is fairly low for XR6, Inspire 2 and P4P, and two to three times higher for the Mavic Pro.

Similar results (StD = 0.10–0.25 m) were be observed by Gindraux et al. (2017) in a UAS survey over glaciated areas with a 12MP sensor (global shutter), mounted on a fixed-wing UAS (Sensefly eBee). The effect of overestimated *z*-values in photogrammetric DEMs was also observed by Salach et al. (2018), who analysed the accuracy of photogrammetric DEMs obtained with a Sony α6000 camera (same camera system as in the present study) on a MSP Hawk Moth multi-copter, a system comparable to the XR6. However, their approach yielded an RMSE of 0.14 m (approximately seven times GSD) that is quite high compared to the XR6 data but comparable to the accuracies obtained with our Mavic system. We assume differences in survey design (only two flight lines with a mean flight height of 50 m above ground), low image overlaps (70% front and 50% sidelap) and consequently few image observations per tie point, but also differences in surface texture and structure to be responsible for the higher RMSE in Salach et al. (2018).

To make the results more comparable and widely applicable, we calculated a RMSE/GSD ratio (Müller et al., 2014) for all data (Table 8). RMSE/GSD ratios are comparable for the XR6, Inspire 2 and Phantom 4 Pro+ (three times GSD) but approximately two times higher for the Mavic Pro data. We therefore conclude that the discrepancies observed in the StD of our data are caused by a lower GSD (Mosbrucker et al., 2017) and poor BA results of the Mavic Pro data when compared to the GSD obtained with the other UAS

TABLE 7 Statistical properties of all data (MAE = mean absolute error, ME = mean eror)

	XR6			Inspire 2			Phantom 4 Pro+			Mavic Pro		
	PA	CG	CGC	PA	CG	CGC	PA	CG	CGC	PA	CG	CGC
RMSE [m]	0.05	0.051	0.053	0.061	0.053	0.061	0.052	0.053	0.055	0.162	0.169	0.124
MAE [m]	0.034	0.035	0.038	0.046	0.039	0.046	0.038	0.038	0.041	0.126	0.132	0.099
ME [m]	−0.004	−0.006	−0.008	−0.015	−0.014	−0.018	−0.009	−0.006	−0.013	−0.039	−0.043	−0.029
T-test (eff.)	−0.08	−0.11	−0.15	−0.25	−0.27	−0.31	−0.18	−0.11	−0.25	−0.24	−0.26	−0.24
T-test (p)	0.35	0.18	0.07	0	0	0	0.03	0.17	0	0	0	0
Median [m]	−0.004	−0.007	−0.003	−0.022	−0.011	−0.016	−0.01	−0.005	−0.011	−0.011	−0.032	−0.014
StD [m]	0.05	0.05	0.053	0.059	0.051	0.058	0.052	0.053	0.053	0.158	0.164	0.12
Skewness	1.483	1.456	0.639	1.019	0.741	0.417	1.147	1.065	0.539	−0.361	−0.311	−0.324
Kurtosis	5.928	5.986	4.145	2.27	2.551	0.945	3.926	3.471	1.442	−0.24	0.029	−0.242
KS test	0	0	0.001	0	0	0.125	0.001	0.034	0.049	0.003	0.315	0.037

TABLE 8 RMSE/GSD ratio

	RMSE/GSD		
UAS	PA	CG	CGC
Mavic Pro	6.4	7.1	4.9
Phantom 4 Pro+	2.6	2.7	2.5
Inspire 2/Zenmuse X4s	3.0	2.8	2.9
XR6/α6000	3.2	3.6	3.4

(Figure 8). This underlines the importance of appropriate survey planning, adjusted to the performance of the respective UAS, in order to meet the requirements for reliable (self-)calibration in SfM processing. Different sensors might require different survey designs (Carbonneau & Dietrich, 2017) and processing strategies to enable reliable photogrammetric image network performance (James et al., 2019) and to accurately determine lens distortion parameters (Fraser, 2001). We also investigated whether more aggressive filtering of error-prone tie points improves the accuracy of the Mavic Pro data to arrive at point cloud accuracies comparable to the other tested UAS. Therefore, we increased the thresholds in the filter operations in the tie-point gradual selection within Photoscan Pro. However, the filtering process did not increase the point cloud accuracy and the GCP-RMSE increased by approximately 10 cm for all data.

3.2.2 | Significant differences from zero

Under a significance level of 0.05, the mean errors of all XR6 data and those of the Phantom 4 Pro+ for the CG flight pattern are not significantly different from zero, and hence do not suggest the presence of a systematic error. For the other flights, the Cohen effect size was between −0.31 and −0.24 and suggests a negligible to weak effect, which means that statistical significance does not necessarily point to a relevant systematic error in these cases. Concerning systematic errors, the Mavic Pro system stands out, with mean errors between −2.9 and −4.3 cm, while all other systems have considerably smaller mean errors between −0.4 and −1.8 cm. Median errors are in the range between −0.3 cm (XR6/CGC) and −3.2 cm (Mavic Pro/CG).

3.2.3 | Normal distribution of errors

P-values for all of the Komolgorov–Smirnov tests were low, suggesting that deviation of the differences from a normal distribution was significant, except for Mavic Pro CG and Inspire 2 CGC data. The general assumption of Gaussian-distributed errors was rejected. The QQ plots (Figure 10) show the quantiles of the observed error distribution plotted against the theoretical quantiles of the respective normal distribution and reveal a deviation from the normal distribution, especially in the upper quantiles. In the case of normally distributed errors, the QQ plots would yield a straight line.

An evaluation of excess kurtosis reveals that almost all distributions that deviate from the normal distribution are leptokurtic. This implies heavier tails than the normal distribution, so a higher influence of outliers. Having verified the assumption of equal variances (Levene test), we conducted one-way ANOVA to investigate significant differences (i) between the three flight patterns for each UAS and (ii) between the four UAS for each flight pattern. According to the results, the mean does not differ significantly among flight patterns for the same UAS. Conversely, there were significant differences between the Mavic and other UAS for the PA and CG flight patterns and no significant differences between UAS for the CGC pattern.

3.2.4 | Spatial autocorrelation

All UAS except Mavic Pro show a 'pure nugget' variogram of measured differences (Figure 11), suggesting spatially uncorrelated random errors. Higher semivariances at a range of 135 m indicate slightly tilted surfaces in all data. We noted a slight variability of semivariances with UAS and flight pattern, but it has to be emphasized that the differences are less than 2 mm at all ranges, thus negligible. In contrast, the Mavic Pro data show much higher variability of semivariances up to 3.9 cm and at the full range of spatial lag trends (i.e. differences increase with distance; indicative for doming).

Generally, we expected a stronger impact of flight patterns on spatial autocorrelation. We assume that the discrepancies between our results and those of other studies are caused by different flight configurations. While Nesbit and Hugenholtz (2019) integrated the nadir flights with oblique images from single and double-convergent

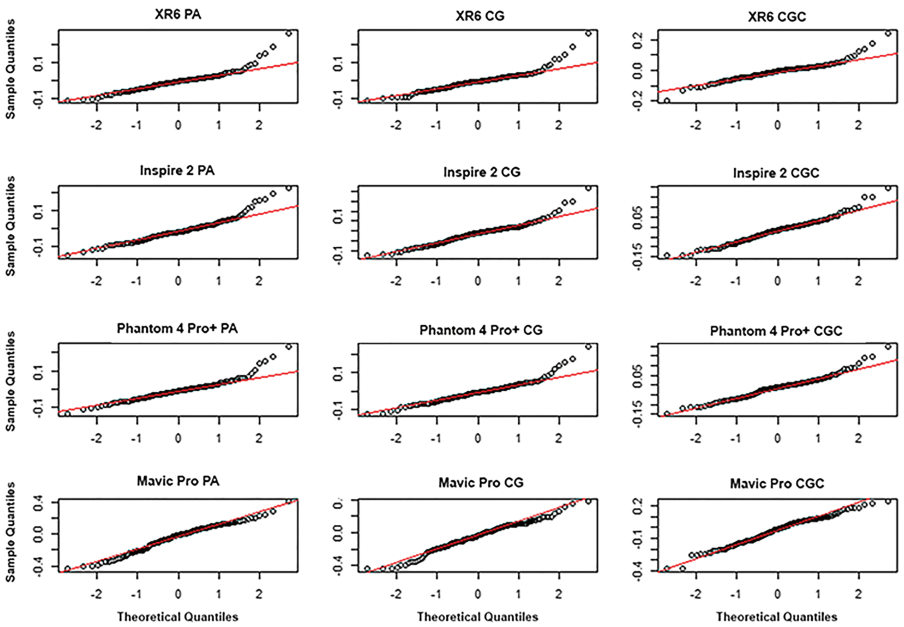

FIGURE 10 QQ plots showing the distribution of errors (black circles) and the theoretical quantiles of their normal distribution (red line) [Color figure can be viewed at wileyonlinelibrary.com]

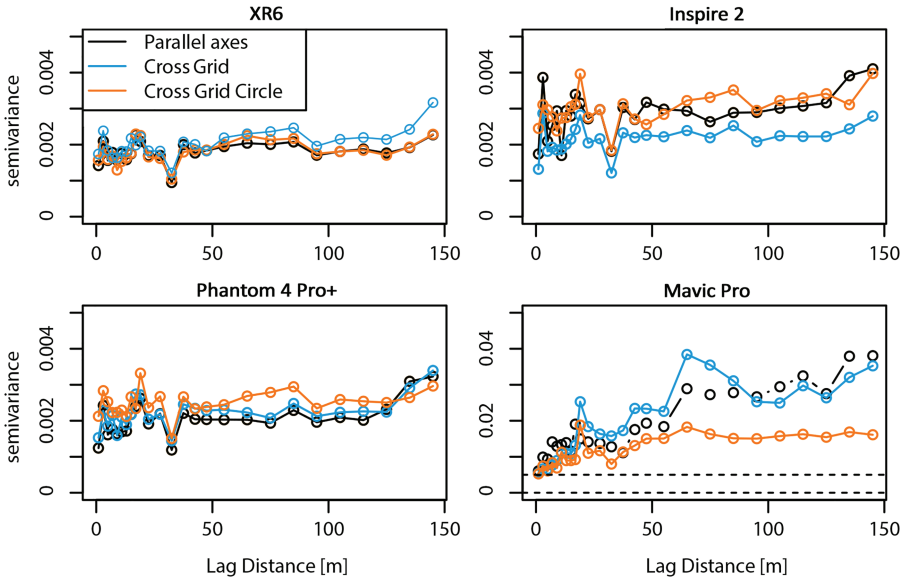

FIGURE 11 Semivariances of differences between CP and DEMs (note that the Mavic Pro diagram has a 10-fold range of semivariances compared to all other diagrams) [Color figure can be viewed at wileyonlinelibrary.com]

arcs, we examined the integration of images acquired during a single point of interest flight with a camera roll angle of 35° and a fixed camera orientation towards the centre of the area of interest in each image. As a result, oblique images do not overlap with vertically oriented images. Nevertheless, from the literature (e.g. Nesbit & Hugenholtz, 2019; Sanz-Ablanedo et al., 2020) we know that if appropriate camera angles and overlapping convergent arc patterns are chosen, the integration of oblique images into a set of (near) nadir images serves for a better lens calibration in the BA and improves the accuracy and precision of the point cloud (Jaud et al., 2019). The Mavic Pro CGC semivariogram could also be interpreted in terms of spatial autocorrelation within a 60 m range if oblique images are included. This behaviour is only visible with the Mavic Pro data.

Spatially correlated errors need to be treated differently than random errors (Rolstad et al., 2009) as they tend to increase with an increasing number of measurements in multi-temporal analysis (Anderson, 2019). On a very small sub-area (spatial extent < 60 m), this could have the same consequences as a survey-wide systematic error, but if the survey area is large compared to the autocorrelation range, the uncertainty will eventually cancel out (Anderson, 2019). Concerning spatial autocorrelation, we have to keep in mind that the main source of systematic errors in photogrammetric products is the sensor (Roth et al., 2018). Nevertheless, the superior performance of the α6000 was also demonstrated by DxOMarks' lab tests, which revealed a huge dynamic range of 13.1 EV and a signal-to-noise ratio three times greater than a P4P (12.5 EV) or Inspire 2/X4s (12.6 EV) (DxOMark, n.d.).

The spatial structure of the XR6, Inspire 2 and Phantom 4 Pro + semivariances could also be interpreted as cyclical (although not distinctive), also described as a 'wave hole effect variogram' (Pereira et al., 2017). The influence of terrain characteristics on DEM errors (Kraus et al., 2006; Müller et al., 2014) could be a possible explanation for the slight intermittency of the semivariances. To verify this hypothesis, we conducted correlation analysis with a focus on the terrain factors of slope, roughness and general curvature.

TABLE 9 Correlation coefficients of signed and unsigned differences and geofactors (unless denoted by 'n.sgin.'; correlations are significant at $\alpha = 0.05$)

		Signed differences			Unsigned differences		
UAS	Flight pattern	Slope	General curvature	Roughness	Slope	General curvature	Roughness
XR6	PA	−0.173	0.518	n.sign.	0.378	−0.138	0.458
XR6	CG	−0.203	0.496	n.sign.	0.409	−0.144	0.387
XR6	CGC	−0.196	0.532	n.sign.	0.403	−0.210	0.464
Inspire 2	PA	−0.229	0.546	n.sign.	0.226	−0.347	0.219
Inspire 2	CG	−0.243	0.549	n.sign.	0.398	−0.300	0.396
Inspire 2	CGC	−0.197	0.630	n.sign.	0.429	−0.325	0.536
Phantom 4 Pro+	PA	−0.197	0.544	n.sign.	0.350	−0.190	0.368
Phantom 4 Pro+	CG	−0.207	0.586	n.sign.	0.389	−0.175	0.436
Phantom 4 Pro+	CGC	−0.223	0.628	n.sign.	0.445	−0.279	0.541
Mavic Pro	PA	n.sign.	0.238	−0.148	n.sign.	−0.141	n.sign.
Mavic Pro	CG	n.sign.	0.273	−0.150	n.sign.	n.sign.	n.sign.
Mavic Pro	CGC	n.sign.	0.433	n.sign.	0.210	−0.169	0.360

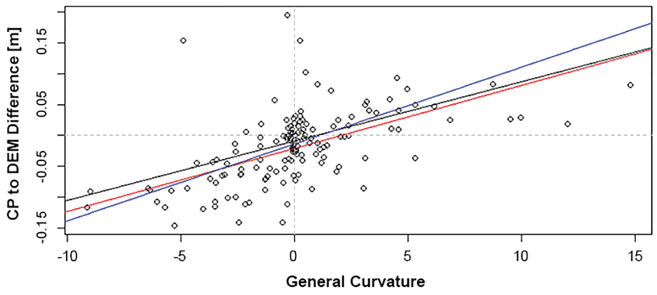

FIGURE 12 Correlation of Inspire 2 data with general curvature [°] of the strongest correlation in Table 9 ($R^2 = 0.6$) with ordinary least squares (black) and robust (red, blue) trend lines [Color figure can be viewed at wileyonlinelibrary.com]

3.2.5 | Correlation with terrain factors

The correlation analyses (*p*-values not corrected for multiple testing) yielded the following results: slope and curvature were correlated with both unsigned and signed differences, but with different strengths and signs (Table 9). A general observation is that curvature correlates more strongly with signed and slope with unsigned differences. Concave surfaces tend towards negative differences, whereas convex areas tend towards positive differences and flat parts show differences around zero (Figure 12). Roughness shows a weak correlation with the magnitude of unsigned differences. The correlation between Mavic Pro differences and terrain properties is either insignificant or weaker than with other UAS. Here, we assume relatively high errors in all parts of the study site to mask the correlation with terrain factors. This assumption was confirmed by further analysis, such as by the differencing of Mavic Pro and a reference DEM.

The correlations between slope inclination and DEM errors are not as strong as the reported correlations of other studies. Scheidl et al. (2008), for example, analysed the dependence of DEM errors (airborne LiDAR) on slope inclination. They found quadratic relationships with r^2 around 0.9 that led to a conspicuous increase of errors beyond 40° of slope. Müller et al. (2014) confirmed those results for the case of photogrammetric DEMs and identified slope inclination as the main factor that determines DEM accuracy. Furthermore, the authors proved that errors increase significantly in areas steeper than 45°. The fact that 95% of CPs in our study are located on slopes with less than 35.5° inclination may serve as an explanation of why the dependence of DEM uncertainty on slope inclination is not as strong as observed by Scheidl et al. (2008). The correlations found here are in contrast to our findings (spatial autocorrelation), which can be explained by the facts that (i) the semivariance only reflects unsigned differences and (ii) the autocorrelation ranges of the analysed terrain factors and those of the measured differences may not be the same.

3.3 | Repeated measurements

To develop an understanding of the magnitude and spatial structure of errors in our data, we aim at a comparative error assessment based on repeated measurements under stable environmental circumstances, where the true change is assumed to be zero. Therefore, the entire study site can be interpreted as stable and all the differences can be considered as measurement differences.

ICP adjustments for the Inspire 2 data produced slightly larger differences (Table 10) and the corresponding histogram reflects a Poisson distribution with a majority of values in the negative range (Figure 13). After co-registration, the histogram of the XR6/Phantom 4 Pro+ DoD changed from a bimodal distribution to a right-skewed distribution with a relatively low peak and a larger spread. StD and mean are comparable to those of the XR6/Inspire 2 DoD. Besides, the flat area in the northwest of the area of interest (higher differences in the Phantom 4 Pro+ DoD), the spatial structure of the Inspire 2 and Phantom 4 Pro+ DoD is quite similar. Compared to the Inspire 2 and Phantom 4 Pro+ DEMs, the Mavic Pro DEM shows clearly higher differences and StD, which could be drastically reduced by co-registration procedures from 11.1 to 1.2 cm and from 16.1 to 7.5 cm, respectively. Thus, the offsets caused by surveying with individual UAS could be negligible for a large number of geomorphological applications (from landscape to catchment scale).

TABLE 10 DoD standard deviation and mean error before and after ICP registration (I2 = Inspire 2; P4P+ = Phantom 4 Pro+; MP = Mavic Pro)

	Before ICP				After ICP			
UAS	Mean [m]	σ [m]	Median [m]	RMSE [m]	Mean [m]	σ [m]	Median [m]	RMSE [m]
XR6/I2	−0.009	0.030	−0.007	0.031	−0.016	0.034	−0.013	0.038
XR6/P4P+	−0.009	0.040	−0.013	0.041	−0.009	0.038	−0.007	0.039
XR6/MP	−0.111	0.161	−0.103	0.195	−0.012	0.075	−0.004	0.076

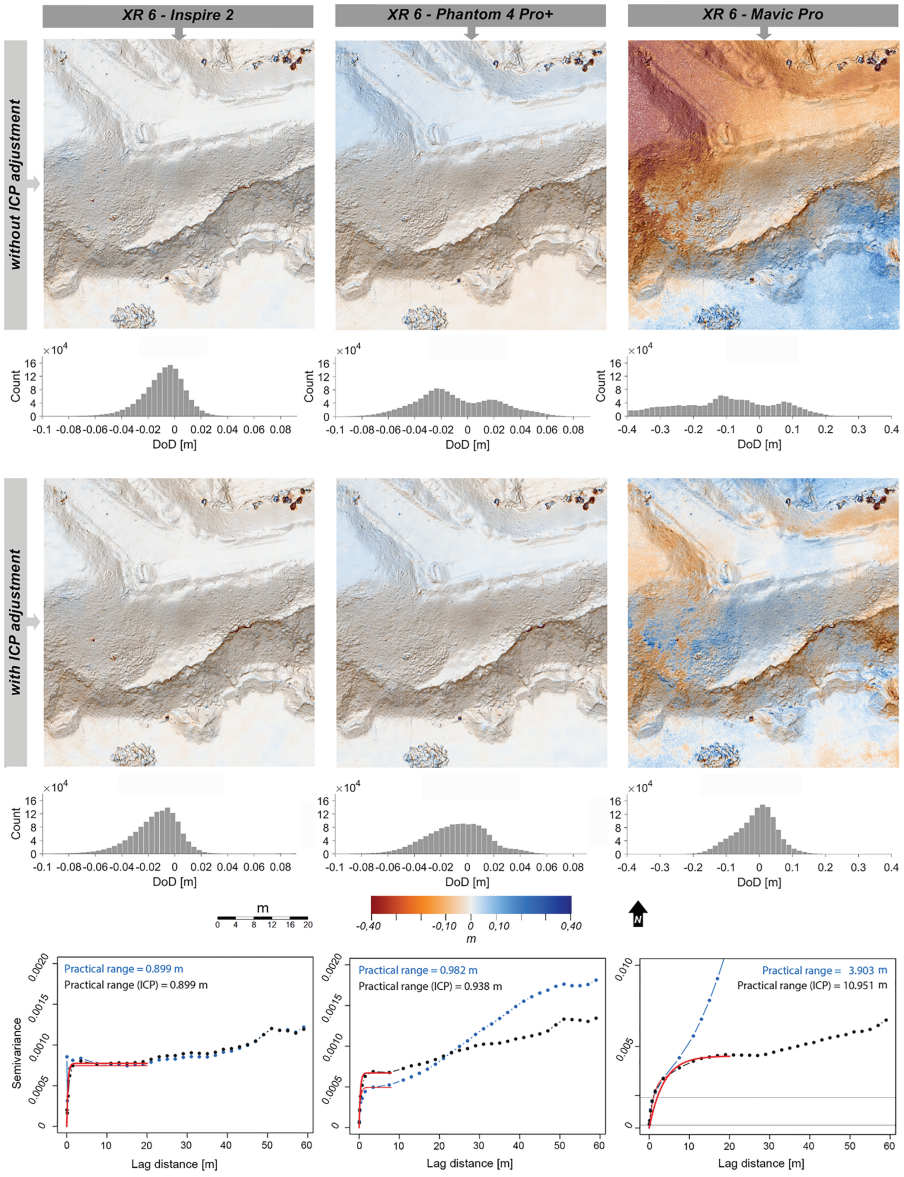

FIGURE 13 CG-DoDs with histograms before (top) and after ICP adjustments (middle) (reference: XR6 CG-DEM) and respective semivariograms (bottom). Note that in the XR6/Mavic Pro semivariogram the semivariances above 15 m lag distance are not shown for graphical reasons (limit of y-axis) [Color figure can be viewed at wileyonlinelibrary.com]

Semivariogram analyses revealed no spatial dependence of DoD values above a distance of 0.9 m for the XR6/Inspire 2 and XR6/Phantom 4 Pro+ calculations. For these two datasets, ICP adjustments had no relevant effect on the spatial dependency of the variables, whereas in the case of the XR6/Phantom 4 Pro+ a clear minimization of both value range and tilt effect (indicated by the strong trend in the semivariograms) is evident. The phenomenon of tilted DEM surfaces and the effect of ICP procedures becomes even more evident in the XR6/Mavic Pro DoDs. Here, the semivariogram shows that variables are spatially dependent at all distances before and up to a distance of 11 m after co-registration of point clouds. A slight cyclic pattern points towards spatial structure in all DoDs, but it is more evident in the case of XR6/Inspire 2 and less distinct in the DoD of XR6/Mavic Pro. We have already shown that differences are correlated with terrain properties; this correlation is reflected in the spatial autocorrelation shown here. The latter has a range (0.9 m) that is well below the smallest distance between CPs, so that it is not shown in the semivariograms of the above 'Spatial autocorrelation' section. A relative peak at a distance of approximately 50 m indicates a slight dome effect (Eltner & Schneider, 2015) in the peripheral parts (outer 10 m) of all DoDs. In the case of the XR6/Mavic Pro DoD, the dome effect is masked by an overall trend pointing towards slightly tilted surfaces in the Mavic Pro DEM.

Surveying from multiple altitudes would have resulted in a higher variation in image scale and consequently would have helped to mitigate the dome effect, as shown by many authors (e.g. Sanz-Ablanedo et al., 2020). However, the study design is based on a uniform survey height for all UAS and so we refrain from surveying from multiple altitudes.

The differencing of DEMs obtained with different UAS revealed non-Gaussian-distributed errors of different magnitude in all DoDs, so the use of different UAS within comparisons should be avoided if possible. This represents a challenge as all technologies evolve, which inevitably means that some models will be withdrawn from the market, as has already happened with Inspire 2 (now equipped with a X5s or X7 camera) and Mavic Pro. The follow-up models (Mavic Air 2, Mavic 2 Pro and DJI Mini 2) are also equipped with rolling shutters, so the results presented may be relevant to those systems as well. Based on the results of Kersten et al. (2020), who carried out comparative accuracy analysis between a P4P, a Zenmuse X5 and an Inspire 2/X4s, we assume no substantial difference in the sensor quality/performance between the X4s and X5s cameras. This assumption is confirmed by the results of DxOmark lab tests, which yielded only marginal higher dynamic range for the X5s (12.7 EV) but a large improvement of EV in the X7 (13.9), which allows more entropy/detail in image content.

4 | CONCLUSION

UAS-SfM has emerged as a very user-friendly method for generating high-resolution DEMs for geomorphological analysis. This study presents a comparative analysis of four different UAS examining the differences in point cloud accuracies derived from different flight patterns. Furthermore, we investigated the influence of terrain factors on DEM accuracy and showed how the use of varying UAS in multi-temporal surveys affects the quality of the DoD.

Our analysis revealed different magnitudes but identical direction of errors in all data. The differences and spread of random errors are remarkably similar for all flight patterns of each UAS. Systematic errors occur, but Cohen's effect sizes suggest a negligible effect, so it does not necessarily indicate a relevant systematic error. Our results clearly separate the Mavic Pro UAS from the XR6, Inspire 2 and Phantom 4 Pro+ systems in terms of random and systematic errors, but also in terms of spatial autocorrelation of errors.

The main sources of the discrepancies between the Mavic Pro data and all other systems are the higher GSD and weak modelling of lens distortion. This can be attributed to (a) rolling shutter effects, even if rolling shutter compensations are applied in the SfM process and (b) a higher degree of on-board image pre-processing as observed by James et al. (2020).

Overall, this study has demonstrated that the survey designs used here could not be guaranteed to work for all UAS to the same degree. If the use of varying UAS in multi-temporal surveys cannot be avoided, operators should focus on achieving a consistent GSD for all flight systems (Mosbrucker et al., 2017) and determine flight height as part of a careful initial survey design. In general, we consider the survey design as the most crucial factor influencing the data accuracy of a respective UAS. Not every survey strategy might be suitable for the purpose of calibrating a specific UAS camera and, depending on the quality of the sensor and the intended purpose, the acquisition strategy can vary widely. In other words, the survey design has to be adapted to the respective UAS and a careful inspection of the BA results, such as high correlation between internal orientation parameters or high image residuals (lens calibration), should always be performed for a first quality assessment of the results. It is worth mentioning that the offsets reported here, caused by surveying with different UAS (StD between 3.4 and 7.5 cm), might be negligible for a large number of geomorphological applications. Our results showed that consumer-grade UAS (here Phantom 4 Pro+) can produce results comparable to the reported accuracies of professional to enterprise-grade UAS, but that accuracies depend on the chosen data sampling strategy and processing parameters. Therefore, surveys should be planned so that they can deliver the data required for the particular geomorphological question being asked.

ACKNOWLEDGEMENTS

We would like to sincerely thank geo-konzept GmbH for the support of this research and for providing the Inspire 2/X4s system. The authors also thank Stuart Lane, Mike James, Patrice Carbonneau, Adam Mosbrucker and one anonymous reviewer for constructive comments on the initial submitted version, which significantly helped to improve the manuscript.

CONFLICT OF INTEREST

The authors declare no conflict of interest.

AUTHOR CONTRIBUTIONS

Manuel Stark took part in conceptualization, methodology (including methodological development), investigation (e.g. data collection), supervision and writing—initial draft and reviewing/editing. Tobias Heckmann contributed in terms of methodology (including methodological development), resources (provision of data, etc.), supervision and writing—initial draft and reviewing/editing. Livia Piermattei contributed in terms of methodology (including methodological development), resources (provision of data, etc.) and reviewing/editing. Fabian Dremel and Patrick Machowski contributed in terms of investigation (e.g. data collection) and resources (provision of data, etc.). Andreas Kaiser assisted with reviewing and editing. Florian Haas assisted with writing—initial draft and reviewing/editing. Michael Becht contributed in terms of funding acquisition, software (provision and development) and supervision.

DATA AVAILABILITY STATEMENT

The presented data is part of DFG Grant HA5740/3–1 and SCHM 1373/8–1 and will be used for the continuation of the project (DFG proposal 'REGIME 4D'/in preparation). It is therefore not publicly available.

ORCID

Manuel Stark https://orcid.org/0000-0001-5014-2881
Tobias Heckmann https://orcid.org/0000-0002-1495-4214

REFERENCES

Anderson, S.W. (2019) Uncertainty in quantitative analyses of topographic change: Error propagation and the role of thresholding. *Earth Surface Processes and Landforms*, 44(5), 1015–1033. https://doi.org/10.1002/esp.4551.

Besl, P. & McKay, N.D. (1992) Method for registration of 3-D shapes. In: *Sensor Fusion IV: Control Paradigms and Data Structures*. Bellingham, WA: International Society for Optics and Photonics, pp. 586–606.

Capolupo, A., Saponaro, M., Borgogno Mondino, E. & Tarantino, E. (2020) Combining interior orientation variables to predict the accuracy of Rpas–Sfm 3D models. *Remote Sensing*, 12(17), 2674. https://doi.org/10.3390/rs12172674.

Carbonneau, P.E. & Dietrich, J.T. (2017) Cost-effective non-metric photogrammetry from consumer-grade sUAS: Implications for direct georeferencing of structure from motion photogrammetry. *Earth Surface Processes and Landforms*, 42(3), 473–486. https://doi.org/10.1002/esp.4012.

Carrivick, J.L., Smith, M.W. & Quincey, D.J. (2016) *Structure from Motion in the Geosciences*. Chichester: Wiley.

Colomina, I. & Molina, P. (2014) Unmanned aerial systems for photogrammetry and remote sensing: A review. *ISPRS Journal of Photogrammetry and Remote Sensing*, 92, 79–97. https://doi.org/10.1016/j.isprsjprs.2014.02.013.

Cook, K.L. (2017) An evaluation of the effectiveness of low-cost UAVs and structure from motion for geomorphic change detection. *Geomorphology*, 278, 195–208. https://doi.org/10.1016/j.geomorph.2016.11.009.

DxOMark Lab Tests. n.d. https://www.dxomark.com/dxomark-benchmarks-for-popular-drone-camera-sensors [accessed 23 November 2020].

Eltner, A., Kaiser, A., Castillo, C., Rock, G., Neugirg, F. & Abellán, A. (2016) Image-based surface reconstruction in geomorphometry – merits, limits and developments. *Earth Surface Dynamics*, 4(2), 359–389. https://doi.org/10.5194/esurf-4-359-2016.

Eltner, A. & Schneider, D. (2015) Analysis of different methods for 3D reconstruction of natural surfaces from parallel-axes UAV images. *The Photogrammetric Record*, 30(151), 279–299. https://doi.org/10.1111/phor.12115.

Federal Network Agency of Germany. (2019) https://www.netzausbau.de/SharedDocs/Downloads/DE/Publikationen/BroschuereFreileitungen.pdf?blob=publicationFile [accessed 25 November 2020].

Fraser, C.S. (2001) Photogrammetric camera component calibration: A review of analytical techniques. In: Huang, G. (Ed.) *Calibration and Orientation of Cameras in Computer Vision*. Berlin: Springer, pp. 95–121.

Gerke, M. & Przybilla, H.J. (2016) Accuracy analysis of photogrammetric UAV image blocks: Influence of onboard RTK-GNSS and cross flight patterns. *Photogrammetrie-Fernerkundung-Geoinformation*, 2016(1), 17–30. https://doi.org/10.1127/pfg/2016/0284.

German Federal Ministry of Transport and Digital Infrastructure. (2020) https://www.bmvi.de/SharedDocs/DE/Artikel/LF/drohnen.html [accessed 25 November 2020].

Gindraux, S., Boesch, R. & Farinotti, D. (2017) Accuracy assessment of digital surface models from unmanned aerial vehicles' imagery on glaciers. *Remote Sensing*, 9(2), 186. https://doi.org/10.3390/rs9020186.

Gross, J. & Ligges, U. (2015) *nortest*: Tests for normality. R Package Version 1.0-4.

Gruen, A. & Beyer, H.A. (2001) System calibration through self-calibration. In: *Calibration and Orientation of Cameras in Computer Vision*. Berlin: Springer, pp. 163–193.

Hamshaw, S.D., Engel, T., Rizzo, D.M., O'Neil-Dunne, J. & Dewoolkar, M. M. (2019) Application of unmanned aircraft system (UAS) for monitoring bank erosion along river corridors. *Geomatics, Natural Hazards and Risk*, 10(1), 1285–1305. https://doi.org/10.1080/19475705.2019.1571533.

Harwin, S. & Lucieer, A. (2012) Assessing the accuracy of georeferenced point clouds produced via multi-view stereopsis from unmanned aerial vehicle (UAV) imagery. *Remote Sensing*, 4(6), 1573–1599. https://doi.org/10.3390/rs4061573.

Haas, F., Hilger, L., Neugirg, F., Umstädter, K., Breitung, C., Fischer, P., *et al*. (2016) Quantification and analysis of geomorphic processes on a recultivated iron ore mine on the Italian island of Elba using long-term ground-based lidar and photogrammetric SfM data by a UAV. *Natural Hazards and Earth System Sciences*, 16(5), 1269–1288. https://doi.org/10.5194/nhess-16-1269-2016.

Hendrickx, H., Vivero, S., De Cock, L., De Wit, B., De Maeyer, P., Lambiel, C., *et al*. (2019) The reproducibility of SfM algorithms to produce detailed Digital Surface Models: The example of PhotoScan applied to a high-alpine rock glacier. *Remote Sensing Letters*, 10(1), 11–20. https://doi.org/10.1080/2150704X.2018.1519641.

Hoaglin, D.C., Mosteller, F. & Tukey, J.W. (1983) *Understanding Robust and Exploratory Data Analysis*. Chichester: Wiley.

Höhle, J. & Höhle, M. (2009) Accuracy assessment of digital elevation models by means of robust statistical methods. *ISPRS Journal of Photogrammetry and Remote Sensing*, 64(4), 398–406. https://doi.org/10.1016/j.isprsjprs.2009.02.003.

James, M.R., Antoniazza, G., Robson, S. & Lane, S.N. (2020) Mitigating systematic error in topographic models for geomorphic change detection: Accuracy, precision and considerations beyond off-nadir imagery. *Earth Surface Processes and Landforms*, 45(10), 2251–2271. https://doi.org/10.1002/esp.4878.

James, M.R., Chandler, J.H., Eltner, A., Fraser, C., Miller, P.E., Mills, J.P., *et al*. (2019) Guidelines on the use of structure-from-motion photogrammetry in geomorphic research. *Earth Surface Processes and Landforms*, 44(10), 2081–2084. https://doi.org/10.1002/esp.4637.

James, M.R. & Robson, S. (2014) Mitigating systematic error in topographic models derived from UAV and ground-based image networks. *Earth Surface Processes and Landforms*, 39(10), 1413–1420. https://doi.org/10.1002/esp.3609.

James, M.R., Robson, S., d'Oleire-Oltmanns, S. & Niethammer, U. (2017a) Optimising UAV topographic surveys processed with structure-from-motion: Ground control quality, quantity and bundle adjustment. *Geomorphology*, 280, 51–66. https://doi.org/10.1016/j.geomorph.2016.11.021.

James, M.R., Robson, S. & Smith, M.W. (2017b) 3-D uncertainty-based topographic change detection with structure-from-motion photogrammetry: Precision maps for ground control and directly georeferenced surveys. *Earth Surface Processes and Landforms*, 42(12), 1769–1788. https://doi.org/10.1002/esp.4125.

Jaud, M., Letortu, P., Théry, C., Grandjean, P., Costa, S., Maquaire, O. & Le Dantec, N. (2019) UAV survey of a coastal cliff face – selection of the best imaging angle. *Measurement*, 139, 10–20. https://doi.org/10.1016/j.measurement.2019.02.024.

Kasprzak, M., Jancewicz, K. & Michniewicz, A. (2018) UAV and SfM in detailed geomorphological mapping of granite tors: An example of Starościńskie Skały (Sudetes, SW Poland). *Pure and Applied Geophysics*, 175(9), 3193–3207. https://doi.org/10.1007/s00024-017-1730-8.

Kersten, T., Schlömer, F. & Przybilla, H.J. (2020) Aerotriangulation von UAV-Bilddaten der Zeche Zollern – Die Ergebnisse verschiedener UAV-Systeme und zweier Softwarepakete im Vergleich. In *UAV 2020 – The Sky is the Limit?* Schriftenreihe des DVW, Band 97, Beiträge zum 185. Wißner-Verlag: Augsburg; 121–140.

Koci, J., Jarihani, B., Leon, J.X., Sidle, R.C., Wilkinson, S.N. & Bartley, R. (2017) Assessment of UAV and ground-based structure from motion with multi-view stereo photogrammetry in a gullied savanna catchment. *ISPRS International Journal of Geo-Information*, 6(11), 328. https://doi.org/10.3390/ijgi6110328.

Kraus, K., Karel, W., Briese, C. & Mandlburger, G. (2006) Local accuracy measures for digital terrain models. *The Photogrammetric Record*, 21(116), 342–354. https://doi.org/10.1111/j.1477-9730.2006.00400.x.

Krenz, J., Greenwood, P. & Kuhn, N.J. (2019) Soil degradation mapping in drylands using unmanned aerial vehicle (UAV) data. *Soil Systems*, 3(2), 33. https://doi.org/10.3390/soilsystems3020033.

Lane, S.N., Reid, S.C., Westaway, R.M. & Hicks, D.M. (2004) Remotely sensed topographic data for river channel research: The identification, explanation and management of error. In: Kelly, R.E.J., Drake, N. A. & Barr, S.L. (Eds.) *Spatial Modelling of the Terrestrial Environment*. Chichester: Wiley, pp. 113–136.

Lane, S.N., Westaway, R.M. & Murray Hicks, D. (2003) Estimation of erosion and deposition volumes in a large, gravel-bed, braided river using synoptic remote sensing. *Earth Surface Processes and Landforms*, 28(3), 249–271. https://doi.org/10.1002/esp.483.

Luhmann, T., Fraser, C. & Maas, H.G. (2016) Sensor modelling and camera calibration for close-range photogrammetry. *ISPRS Journal of Photogrammetry and Remote Sensing*, 115, 37–46. https://doi.org/10.1016/j.isprsjprs.2015.10.006.

Milan, D.J., Heritage, G.L., Large, A.R. & Fuller, I.C. (2011) Filtering spatial error from DEMs: Implications for morphological change estimation. *Geomorphology*, 125(1), 160–171. https://doi.org/10.1016/j.geomorph.2010.09.012.

Mosbrucker, A.R., Major, J.J., Spicer, K.R. & Pitlick, J. (2017) Camera system considerations for geomorphic applications of SfM photogrammetry. *Earth Surface Processes and Landforms*, 42(6), 969–986. https://doi.org/10.1002/esp.4066.

Müller, J., Gärtner-Roer, I., Thee, P. & Ginzler, C. (2014) Accuracy assessment of airborne photogrammetrically derived high-resolution digital elevation models in a high mountain environment. *ISPRS Journal of Photogrammetry and Remote Sensing*, 98, 58–69. https://doi.org/10.1016/j.isprsjprs.2014.09.015.

Nesbit, P.R. & Hugenholtz, C.H. (2019) Enhancing UAV–SFM 3D model accuracy in high-relief landscapes by incorporating oblique images. *Remote Sensing*, 11(3), 239. https://doi.org/10.3390/rs11030239.

Neugirg, F., Stark, M., Kaiser, A., Vlacilova, M., Della Seta, M., Vergari, F., *et al*. (2016) Erosion processes in Calanchi in the Upper Orcia Valley, Southern Tuscany, Italy based on multitemporal high-resolution terrestrial LiDAR and UAV surveys. *Geomorphology*, 269, 8–22. https://doi.org/10.1016/j.geomorph.2016.06.027.

Pereira, P., Brevik, E.C., Cerdà, A., Úbeda, X., Novara, A., Francos, M., *et al*. (2017) Mapping ash $CaCO_3$, pH, and extractable elements using principal component analysis. In: Pereira, P., Brevik, E.C., Muñoz-Rojas, M. & Miller, B.A. (Eds.) *Soil Mapping and Process Modeling for Sustainable Land Use Management*. Amsterdam: Elsevier, pp. 319–334.

Piermattei, L., Carturan, L., de Blasi, F., Tarolli, P., Fontana, G.D., Vettore, A. & Pfeifer, N. (2016) Suitability of ground-based SfM-MVS for monitoring glacial and periglacial processes. *Earth Surface Dynamics*, 4(2), 425–443. https://doi.org/10.5194/esurf-4-425-2016.

Przybilla, H.J., Bäumker, M., Luhmann, T., Hastedt, H. & Eilers, M. (2020) Interaction between direct georeferencing, control point configuration and camera self-calibration for RTK-based UAV photogrammetry. *The International Archives of Photogrammetry, Remote Sensing and Spatial Information Sciences*, 43, 485–492. https://doi.org/10.5194/isprs-archives-XLIII-B1-2020-485-20.

Rolstad, C., Haug, T. & Denby, B. (2009) Spatially integrated geodetic glacier mass balance and its uncertainty based on geostatistical analysis: Application to the western Svartisen ice cap, Norway. *Journal of Glaciology*, 55(192), 666–680. https://doi.org/10.3189/002214309789470950.

Rossini, M., Di Mauro, B., Garzonio, R., Baccolo, G., Cavallini, G., Mattavelli, M., *et al*. (2018) Rapid melting dynamics of an alpine glacier with repeated UAV photogrammetry. *Geomorphology*, 304, 159–172. https://doi.org/10.1016/j.geomorph.2017.12.039.

Roth, L., Aasen, H., Walter, A. & Liebisch, F. (2018) Extracting leaf area index using viewing geometry effects – a new perspective on high-resolution unmanned aerial system photography. *ISPRS Journal of Photogrammetry and Remote Sensing*, 141, 161–175. https://doi.org/10.1016/j.isprsjprs.2018.04.012.

Salach, A., Bakuła, K., Pilarska, M., Ostrowski, W., Górski, K. & Kurczyński, Z. (2018) Accuracy assessment of point clouds from LidAR and dense image matching acquired using the UAV platform for DTM creation. *ISPRS International Journal of Geo-Information*, 7(9), 342. https://doi.org/10.3390/ijgi7090342.

Sanz-Ablanedo, E., Chandler, J.H., Ballesteros-Pérez, P. & Rodríguez-Pérez, J.R. (2020) Reducing systematic dome errors in digital elevation models through better UAV flight design. *Earth Surface Processes and Landforms*, 45(9), 2134–2147. https://doi.org/10.1002/esp.4871.

Scheidl, C., Rickenman, D. & Chiari, M. (2008) The use of airborne LiDAR data for the analysis of debris flow events in Switzerland. *Natural Hazards and Earth System Sciences*, 8(5), 1113–1127. https://doi.org/10.3929/ethz-b-000069723.

Stark, M., Neugirg, F., Kaiser, A., Della Seta, M., Schmidt, J., Becht, M. & Haas, F. (2020) Calanchi badlands reconstructions and long-term change detection analysis from historical aerial and UAS image processing. *Journal of Geomorphology*, 1(1), 1–24. https://doi.org/10.1127/jgeomorphology/2020/0658.

Torres-Sánchez, J., López-Granados, F., Borra-Serrano, I. & Peña, J.M. (2018) Assessing UAV-collected image overlap influence on computation time and digital surface model accuracy in olive orchards. *Precision Agriculture*, 19(1), 115–133. https://doi.org/10.1007/s11119-017-9502-0.

Vautherin, J., Rutishauser, S., Schneider-Zapp, K., Choi, H.F., Chovancova, V., Glass, A. & Strecha, C. (2016) Photogrammetric accuracy and modeling of rolling shutter cameras. *ISPRS Annals of Photogrammetry, Remote Sensing & Spatial Information Sciences*, 3(3), 139–146. https://doi.org/10.5194/isprsannals-III-3-139-2016.

Wheaton, J.M., Brasington, J., Darby, S.E. & Sear, D.A. (2010) Accounting for uncertainty in DEMs from repeat topographic surveys: Improved sediment budgets. *Earth Surface Processes and Landforms*, 35(2), 136–156. https://doi.org/10.1002/esp.1886.

Zevenbergen, L.W. & Thorne, C.R. (1987) Quantitative analysis of land surface topography. *Earth Surface Processes and Landforms*, 12(1), 47–56. https://doi.org/10.1002/esp.3290120107.

Zhang, D., Liu, J., Ni, W., Sun, G., Zhang, Z., Liu, Q. & Wang, Q. (2019) Estimation of forest leaf area index using height and canopy cover information extracted from unmanned aerial vehicle stereo imagery. *IEEE Journal of Selected Topics in Applied Earth Observations and Remote Sensing*, 12(2), 471–481. https://doi, https://doi.org/10.1109/JSTARS.2019.2891519.

Zhou, Y., Daakir, M., Rupnik, E. & Pierrot-Deseilligny, M. (2020) A two-step approach for the correction of rolling shutter distortion in UAV photogrammetry. *ISPRS Journal of Photogrammetry and Remote Sensing*, 160, 51–66. https://doi.org/10.1016/j.isprsjprs.2019.11.020.

How to cite this article: Stark M, Heckmann T, Piermattei L, et al. From consumer to enterprise grade: How the choice of four UAS impacts point cloud quality. *Earth Surf. Process. Landforms*. 2021;46:2019–2043. https://doi.org/10.1002/esp.5142

APPENDIX A

TABLE A1 UAS flight heights of recently published studies

Author	Flight height above ground
James et al., 2017a, b)	100 and 20–250 m
Przybilla et al. (2020)	60–80 m
Capolupo et al. (2020)	100 m
Sanz-Ablanedo et al. (2020)	35–65 m
Hendrickx et al. (2019)	95 m
Cook (2017)	35–60 m
Kersten et al. (2020)	50–96 m
James et al. (2020)	50 m
Nesbit and Hugenholtz (2019)	50 m
Zhou et al. (2020)	30–90 m
Gindraux et al. (2017)	115 m
Neugirg et al. (2016)	Approx. 110 m
Haas et al. (2016)	50–80 m

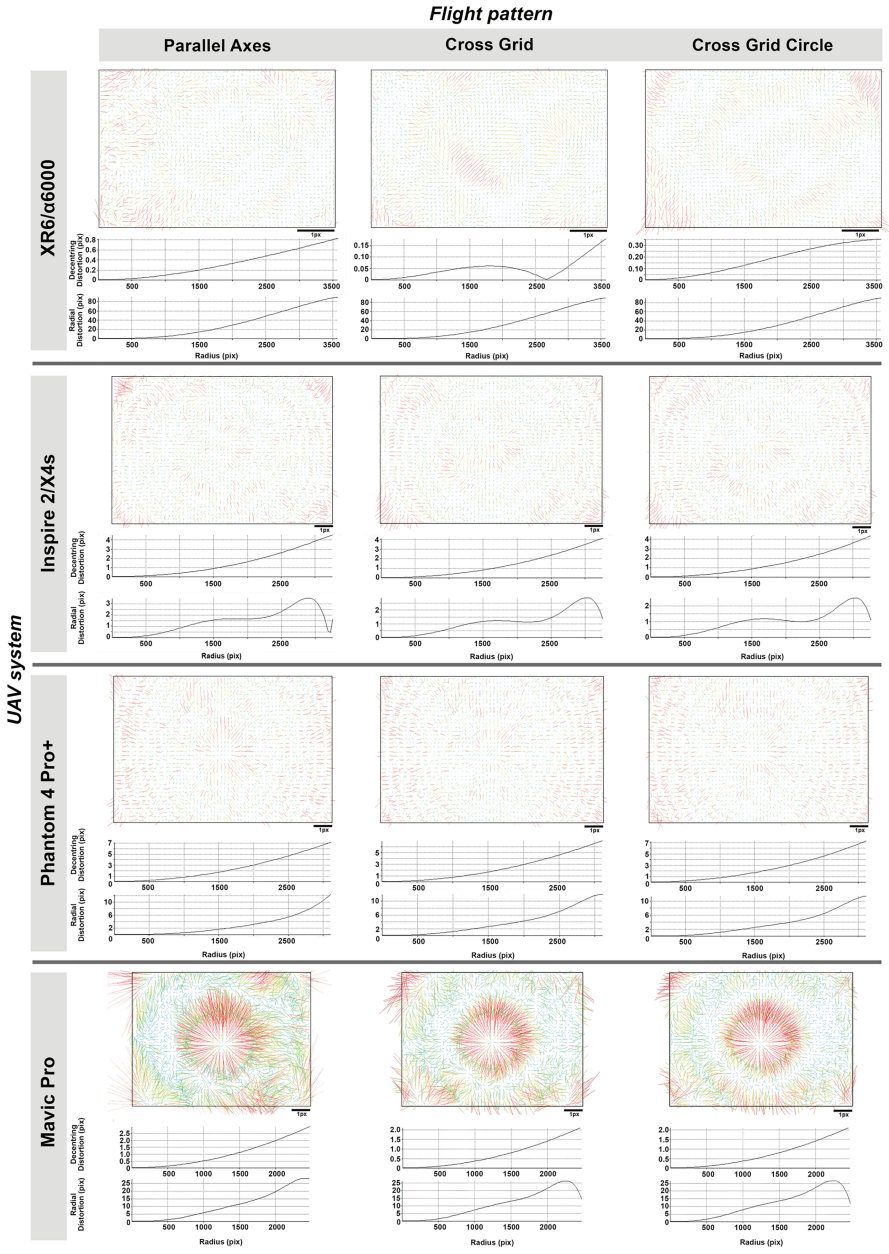

FIGURE A1 Camera residuals after autocalibration with decentring and radial distortion plots. Note the non-uniform scaling of the Y-axes in distortion plots [Color figure can be viewed at wileyonlinelibrary.com]

TABLE A2 Complete list of all GCP and CP StDs (GNSS measurements in RTK mode)

	Coordinates			StD [m]				
ID	X	Y	Z	X	Y	Z	Type	Satellites [count]
1	656 623.192	5 419 163.19	592.258	0.004	0.002	0.007	GCP	13
2	656 629.780	5 419 179.18	592.623	0.004	0.003	0.009	GCP	12
3	656 646.442	5 419 156.90	592.192	0.005	0.004	0.011	GCP	14
4	656 668.790	5 419 150.92	591.634	0.005	0.003	0.01	GCP	15
5	656 698.026	5 419 157.67	591.013	0.006	0.004	0.012	GCP	14
6	656 713.713	5 419 170.70	590.856	0.009	0.009	0.025	GCP	8
7	656 743.792	5 419 161.89	590.292	0.006	0.004	0.012	GCP	14
8	656 774.523	5 419 168.15	589.515	0.006	0.004	0.013	GCP	12
9	656 804.583	5 419 151.30	588.966	0.003	0.002	0.007	GCP	12
10	656 761.308	5 419 191.48	589.853	0.005	0.004	0.014	GCP	12
11	656 691.193	5 419 190.17	595.191	0.009	0.006	0.025	GCP	11
12	656 666.715	5 419 180.82	591.786	0.008	0.006	0.023	GCP	11
13	656 769.972	5 419 239.61	600.793	0.005	0.004	0.012	GCP	13
14	656 749.776	5 419 264.61	600.215	0.006	0.004	0.014	GCP	13
15	656 742.314	5 419 248.43	599.591	0.006	0.004	0.014	GCP	13
16	656 724.067	5 419 277.70	603.595	0.008	0.005	0.021	GCP	12
17	656 714.125	5 419 263.35	603.816	0.008	0.005	0.021	GCP	12
18	656 724.607	5 419 248.25	604.390	0.006	0.005	0.015	GCP	13
19	656 712.843	5 419 249.17	604.626	0.005	0.004	0.012	GCP	12
20	656 695.361	5 419 276.90	603.846	0.008	0.005	0.018	GCP	13
21	656 656.784	5 419 279.61	604.293	0.009	0.006	0.023	GCP	12
22	656 643.585	5 419 263.97	606.597	0.011	0.007	0.029	GCP	12
23	656 657.345	5 419 214.66	609.446	0.009	0.006	0.021	GCP	12
24	656 698.890	5 419 219.71	607.882	0.008	0.006	0.018	GCP	13
25	656 728.995	5 419 227.56	606.593	0.008	0.005	0.017	GCP	13
26	656 756.121	5 419 222.19	606.219	0.008	0.005	0.017	CP	13
27	656 695.988	5 419 186.19	594.141	0.005	0.004	0.009	CP	14
28	656 699.311	5 419 186.40	593.513	0.005	0.003	0.008	CP	15
29	656 702.828	5 419 180.11	590.967	0.005	0.003	0.009	CP	14
30	656 708.432	5 419 174.08	590.870	0.005	0.003	0.009	CP	15
31	656 690.943	5 419 173.65	591.328	0.005	0.003	0.009	CP	14
32	656 684.361	5 419 180.80	591.278	0.005	0.003	0.009	CP	15
33	656 676.978	5 419 187.79	591.743	0.005	0.004	0.009	CP	14
34	656 669.518	5 419 190.20	593.138	0.005	0.004	0.009	CP	14
35	656 667.753	5 419 183.07	591.758	0.005	0.004	0.009	CP	14
36	656 658.510	5 419 178.33	591.998	0.005	0.004	0.009	CP	14
37	656 653.668	5 419 184.10	592.592	0.006	0.004	0.01	CP	14
38	656 651.103	5 419 182.35	592.500	0.006	0.004	0.01	CP	14
39	656 650.194	5 419 185.65	594.212	0.006	0.004	0.01	CP	14
40	656 648.506	5 419 175.14	593.713	0.006	0.004	0.011	CP	14
41	656 650.079	5 419 168.93	591.896	0.005	0.004	0.009	CP	15
42	656 663.318	5 419 171.93	591.769	0.005	0.004	0.009	CP	15
43	656 677.938	5 419 172.37	591.445	0.005	0.004	0.009	CP	15
44	656 688.629	5 419 171.31	591.402	0.005	0.004	0.009	CP	15
45	656 706.185	5 419 170.89	590.799	0.005	0.004	0.009	CP	14
46	656 721.846	5 419 173.72	590.703	0.005	0.004	0.009	CP	15
47	656 730.463	5 419 178.95	590.646	0.005	0.004	0.009	CP	15
48	656 737.982	5 419 196.75	592.757	0.006	0.004	0.011	CP	13

(Continues)

TABLE A2 (Continued)

	Coordinates			StD [m]				
ID	X	Y	Z	X	Y	Z	Type	Satellites [count]
49	656 734.888	5 419 196.04	592.670	0.006	0.004	0.011	CP	13
50	656 725.116	5 419 194.65	592.367	0.009	0.005	0.015	CP	10
51	656 705.424	5 419 197.25	592.998	0.007	0.004	0.012	CP	12
52	656 700.990	5 419 199.59	594.667	0.007	0.004	0.012	CP	11
53	656 695.521	5 419 198.15	593.874	0.007	0.004	0.013	CP	12
54	656 695.115	5 419 194.13	591.865	0.007	0.004	0.012	CP	12
55	656 694.194	5 419 191.28	593.438	0.008	0.005	0.014	CP	12
56	656 700.063	5 419 188.48	591.972	0.006	0.005	0.012	CP	14
57	656 702.819	5 419 186.47	591.299	0.006	0.004	0.011	CP	15
58	656 704.912	5 419 183.69	590.973	0.006	0.004	0.011	CP	14
59	656 709.803	5 419 177.12	590.903	0.006	0.004	0.01	CP	15
60	656 740.056	5 419 167.52	590.313	0.004	0.003	0.008	CP	14
61	656 749.223	5 419 177.58	589.955	0.004	0.003	0.008	CP	14
62	656 754.130	5 419 191.41	589.921	0.005	0.003	0.009	CP	15
63	656 750.358	5 419 198.58	592.494	0.005	0.004	0.011	CP	13
64	656 755.559	5 419 198.98	592.349	0.007	0.004	0.012	CP	10
65	656 757.734	5 419 200.61	592.842	0.006	0.004	0.012	CP	13
66	656 762.527	5 419 200.15	592.327	0.006	0.004	0.012	CP	13
67	656 762.741	5 419 198.83	591.412	0.006	0.004	0.012	CP	12
68	656 772.818	5 419 193.62	589.490	0.006	0.004	0.011	CP	13
69	656 778.104	5 419 199.80	590.211	0.005	0.004	0.01	CP	14
70	656 779.658	5 419 202.48	592.045	0.005	0.004	0.011	CP	14
71	656 811.609	5 419 203.94	592.332	0.006	0.004	0.011	CP	14
72	656 796.590	5 419 215.56	595.131	0.008	0.006	0.015	CP	12
73	656 789.378	5 419 228.53	597.558	0.006	0.004	0.012	CP	13
74	656 776.493	5 419 242.82	600.381	0.012	0.012	0.028	CP	9
75	656 773.982	5 419 242.74	600.516	0.003	0.002	0.007	CP	14
76	656 768.454	5 419 241.29	601.393	0.003	0.002	0.007	CP	14
77	656 763.362	5 419 245.40	601.758	0.003	0.003	0.007	CP	14
78	656 763.232	5 419 247.14	601.319	0.003	0.003	0.007	CP	14
79	656 765.782	5 419 247.10	601.676	0.003	0.003	0.007	CP	14
80	656 760.292	5 419 240.67	601.979	0.004	0.003	0.008	CP	13
81	656 754.815	5 419 236.00	603.248	0.003	0.003	0.007	CP	14
82	656 745.820	5 419 237.98	604.658	0.004	0.003	0.008	CP	13
83	656 745.334	5 419 227.74	606.763	0.005	0.003	0.01	CP	14
84	656 746.163	5 419 223.41	606.062	0.004	0.003	0.008	CP	14
85	656 748.383	5 419 217.33	606.302	0.004	0.003	0.008	CP	14
86	656 755.183	5 419 218.04	605.740	0.004	0.003	0.008	CP	14
87	656 761.460	5 419 219.12	606.143	0.004	0.003	0.008	CP	14
88	656 763.737	5 419 218.94	605.933	0.004	0.003	0.008	CP	14
89	656 738.206	5 419 221.81	606.075	0.004	0.003	0.008	CP	14
90	656 728.034	5 419 216.92	606.521	0.004	0.003	0.008	CP	14
91	656 726.815	5 419 215.35	606.519	0.004	0.003	0.008	CP	14
92	656 725.723	5 419 223.73	606.544	0.004	0.003	0.008	CP	13
93	656 722.464	5 419 229.03	607.238	0.004	0.003	0.008	CP	15
94	656 716.361	5 419 227.94	607.185	0.004	0.003	0.008	CP	15
95	656 713.206	5 419 222.00	607.157	0.004	0.003	0.008	CP	14
96	656 709.902	5 419 215.98	607.587	0.004	0.003	0.008	CP	14

(Continues)

TABLE A2 (Continued)

	Coordinates			StD [m]				
ID	X	Y	Z	X	Y	Z	Type	Satellites [count]
97	656 707.283	5 419 215.67	608.149	0.004	0.003	0.009	CP	14
98	656 700.013	5 419 226.71	608.264	0.004	0.003	0.008	CP	14
99	656 693.715	5 419 221.96	608.038	0.004	0.003	0.008	CP	14
100	656 685.000	5 419 222.39	608.123	0.004	0.003	0.009	CP	14
101	656 683.690	5 419 225.73	608.208	0.004	0.003	0.008	CP	14
102	656 678.239	5 419 220.62	608.289	0.004	0.003	0.008	CP	14
103	656 673.774	5 419 213.51	608.204	0.004	0.003	0.008	CP	13
104	656 665.233	5 419 221.42	608.937	0.004	0.003	0.009	CP	12
105	656 658.037	5 419 218.31	609.501	0.007	0.005	0.015	CP	13
106	656 653.297	5 419 215.78	609.797	0.004	0.003	0.008	CP	14
107	656 650.380	5 419 213.93	610.532	0.004	0.003	0.008	CP	14
108	656 650.832	5 419 211.61	609.991	0.004	0.003	0.008	CP	14
109	656 645.651	5 419 217.68	610.918	0.008	0.005	0.018	CP	6
110	656 643.607	5 419 226.75	611.766	0.004	0.003	0.009	CP	12
111	656 638.798	5 419 235.23	613.236	0.004	0.003	0.01	CP	13
112	656 621.834	5 419 236.72	615.268	0.005	0.003	0.01	CP	12
113	656 619.076	5 419 226.13	615.419	0.006	0.004	0.012	CP	14
114	656 611.816	5 419 239.76	615.557	0.006	0.004	0.013	CP	12
115	656 597.453	5 419 243.98	615.484	0.005	0.004	0.011	CP	14
116	656 607.381	5 419 263.35	616.302	0.007	0.005	0.015	CP	11
117	656 609.793	5 419 261.51	615.331	0.006	0.004	0.011	CP	11
118	656 585.832	5 419 277.93	614.691	0.004	0.003	0.009	CP	11
119	656 577.729	5 419 294.45	613.679	0.007	0.004	0.016	CP	9
120	656 607.003	5 419 299.49	609.914	0.006	0.004	0.012	CP	11
121	656 637.353	5 419 307.57	609.391	0.012	0.007	0.019	CP	12
122	656 643.118	5 419 290.46	608.775	0.009	0.007	0.019	CP	12
123	656 638.440	5 419 274.59	607.232	0.009	0.008	0.022	CP	10
124	656 645.861	5 419 266.72	606.930	0.009	0.007	0.02	CP	11
125	656 641.245	5 419 255.86	606.746	0.075	0.009	0.076	CP	7
126	656 646.262	5 419 247.93	606.020	0.004	0.003	0.008	CP	14
127	656 656.554	5 419 253.55	606.346	0.005	0.004	0.01	CP	14
128	656 657.012	5 419 235.37	605.971	0.016	0.009	0.032	CP	10
129	656 661.422	5 419 235.22	606.702	0.008	0.006	0.015	CP	12
130	656 665.278	5 419 231.58	606.143	0.007	0.005	0.014	CP	13
131	656 666.646	5 419 240.18	604.995	0.011	0.006	0.016	CP	10
132	656 668.221	5 419 230.74	604.649	0.007	0.005	0.015	CP	14
133	656 676.814	5 419 230.00	605.261	0.009	0.005	0.015	CP	12
134	656 678.498	5 419 235.63	605.190	0.008	0.006	0.017	CP	10
135	656 682.103	5 419 240.14	604.920	0.008	0.007	0.017	CP	11
136	656 683.038	5 419 245.16	604.541	0.007	0.005	0.014	CP	13
137	656 703.969	5 419 246.54	604.420	0.01	0.006	0.018	CP	10
138	656 718.230	5 419 241.15	604.536	0.009	0.006	0.016	CP	10
139	656 728.771	5 419 237.76	604.014	0.007	0.005	0.014	CP	13
140	656 722.861	5 419 247.44	604.681	0.007	0.005	0.015	CP	12
141	656 726.829	5 419 249.08	603.984	0.007	0.005	0.014	CP	13
142	656 718.88	5 419 254.58	604.574	0.007	0.005	0.015	CP	13
143	656 707.125	5 419 267.99	603.956	0.007	0.005	0.013	CP	13
144	656 690.901	5 419 279.6	604.903	0.01	0.006	0.017	CP	12

(Continues)

TABLE A2 (Continued)

	Coordinates			StD [m]				
ID	X	Y	Z	X	Y	Z	Type	Satellites [count]
145	656 692.839	5 419 283.89	606.434	0.007	0.005	0.014	CP	13
146	656 692.761	5 419 285.99	606.072	0.006	0.005	0.013	CP	13
147	656 678.4	5 419 283.42	604.074	0.006	0.005	0.013	CP	13
148	656 662.938	5 419 271.04	604.614	0.007	0.006	0.017	CP	10
149	656 654.838	5 419 273.96	604.476	0.013	0.006	0.017	CP	9
150	656 650.426	5 419 274.07	604.643	0.007	0.005	0.014	CP	11
151	656 649.805	5 419 273.54	605.184	0.007	0.005	0.013	CP	12
152	656 649.018	5 419 274.97	605.556	0.007	0.005	0.014	CP	11
153	656 648.052	5 419 275.07	605.272	0.007	0.005	0.014	CP	12
154	656 650.167	5 419 276.29	604.745	0.007	0.005	0.014	CP	12
155	656 652.714	5 419 277.86	604.448	0.007	0.005	0.015	CP	13
156	656 694.741	5 419 258.92	604.115	0.017	0.008	0.033	CP	7
157	656 713.732	5 419 277.07	603.845	0.076	0.012	0.055	CP	10
158	656 741.901	5 419 268.02	603.309	0.004	0.003	0.008	CP	14
159	656 741.539	5 419 270.89	603.393	0.004	0.003	0.008	CP	14
160	656 743.156	5 419 270.98	603.972	0.004	0.003	0.008	CP	14
161	656 741.485	5 419 279.25	603.391	0.006	0.004	0.013	CP	11
162	656 727.544	5 419 259.87	603.291	0.006	0.004	0.012	CP	14
163	656 737.709	5 419 261.86	602.928	0.005	0.004	0.011	CP	14
164	656 745.303	5 419 260.67	601.593	0.004	0.003	0.009	CP	14
165	656 751.714	5 419 262.1	600.302	0.005	0.004	0.01	CP	13
166	656 746.645	5 419 264.81	600.516	0.005	0.004	0.01	CP	13
167	656 753.282	5 419 265.32	600.553	0.004	0.003	0.009	CP	14
168	656 760.315	5 419 257.24	599.657	0.005	0.003	0.009	CP	14
169	656 749.493	5 419 250.96	599.981	0.005	0.004	0.01	CP	14
170	656 742.436	5 419 262.42	600.871	0.005	0.004	0.01	CP	13
171	656 733.01	5 419 257.07	603.143	0.005	0.004	0.01	CP	13
172	656 738.901	5 419 254.36	601.547	0.005	0.003	0.009	CP	13
173	656 737.053	5 419 253.29	601.050	0.004	0.003	0.008	CP	13
174	656 737.787	5 419 252.22	600.376	0.004	0.003	0.008	CP	13
175	656 738.258	5 419 248.63	599.165	0.005	0.003	0.009	CP	13
176	656 736.172	5 419 241.9	599.616	0.007	0.004	0.012	CP	12
177	656 765.726	5 419 251.14	600.213	0.006	0.004	0.011	CP	13
178	656 769.057	5 419 246.99	600.907	0.007	0.005	0.012	CP	11
179	656 752.521	5 419 237.9	603.439	0.006	0.004	0.012	CP	13
180	656 756.421	5 419 235.2	603.884	0.006	0.004	0.011	CP	13
181	656 693.525	5 419 280.47	605.455	0.005	0.003	0.009	CP	12

TABLE A3 Correlation matrix of α6000 camera internal orientation parameters in PA flight mode (f = focal length; X_p and Y_p = coordinates of principal point offset, b_1 and b_2 = skewness; k_1–k_4 = components of radial distortions; p_1 and p_2 = components of decentring distortions)

	f (pix)	X_p (pix)	Y_p (pix)	b_1	b_2	k_1	k_2	k_3	k_4	p_1	p_2
f (pix)	1.00	0.04	−0.01	−0.02	−0.02	−0.22	0.13	−0.10	0.09	−0.01	0.05
X_p (pix)		1.00	−0.13	−0.50	0.10	−0.01	−0.00	0.01	−0.02	−0.21	0.04
Y_p (pix)			1.00	0.04	−0.49	−0.01	0.01	−0.00	0.00	0.17	−0.32
b_1				1.00	0.00	−0.01	−0.00	−0.00	0.00	0.18	0.06
b_2					1.00	0.01	−0.00	0.00	0.00	−0.10	0.38
k_1						1.00	**−0.97**	**0.92**	**−0.87**	−0.02	0.01
k_2							1.00	**−0.99**	**0.96**	0.02	−0.02
k_3								1.00	**−0.99**	−0.02	0.02
k_4									1.00	0.01	−0.01
p_1										1.00	−0.18
p_2											1.00

TABLE A4 Correlation matrix of α6000 camera i.O. parameters in CG flight mode (parameters are described in the caption to Table A3)

	f (pix)	X_p (pix)	Y_p (pix)	b_1	b_2	k_1	k_2	k_3	k_4	p_1	p_2
f (pix)	1.00	−0.28	−0.11	−0.04	−0.03	−0.20	0.13	−0.09	0.08	0.07	0.05
X_p (pix)		1.00	0.30	0.01	0.30	0.02	−0.00	−0.00	0.00	0.14	0.26
Y_p (pix)			1.00	−0.38	0.09	0.01	−0.00	0.00	−0.01	0.29	0.24
b_1				1.00	−0.01	0.03	−0.05	0.04	−0.04	−0.05	−0.03
b_2					1.00	−0.00	0.01	−0.01	0.01	−0.06	−0.03
k_1						1.00	**−0.96**	**0.92**	**−0.87**	−0.06	−0.02
k_2							1.00	**−0.99**	**0.96**	0.04	0.01
k_3								1.00	**−0.99**	−0.03	−0.01
k_4									1.00	0.02	0.01
p_1										1.00	0.66
p_2											1.00

TABLE A5 Correlation matrix of α6000 camera i.O. parameters in CGC flight mode (parameters are described in the caption to Table A3)

	f (pix)	X_p (pix)	Y_p (pix)	b_1	b_2	k_1	k_2	k_3	k_4	p_1	p_2
f (pix)	1.00	−0.04	−0.40	−0.02	−0.07	−0.37	0.35	−0.32	0.30	−0.02	0.12
X_p (pix)		1.00	0.06	−0.06	0.23	−0.01	0.01	−0.00	−0.00	0.55	0.03
Y_p (pix)			1.00	−0.30	0.12	0.03	−0.03	0.03	−0.03	−0.01	0.34
b_1				1.00	−0.03	0.03	−0.04	0.04	−0.03	−0.05	0.05
b_2					1.00	−0.01	0.01	−0.01	0.01	−0.01	−0.05
k_1						1.00	**−0.97**	**0.93**	**−0.88**	−0.02	0.01
k_2							1.00	**−0.99**	**0.96**	0.02	−0.03
k_3								1.00	**−0.99**	−0.01	0.03
k_4									1.00	−0.00	−0.03
p_1										1.00	−0.24
p_2											1.00

TABLE A6 Correlation matrix of Inspire 2/X4s camera i.O. parameters in PA flight mode (parameters are described in the caption to Table A3)

	f (pix)	X_p (pix)	Y_p (pix)	b_1	b_2	k_1	k_2	k_3	k_4	p_1	p_2
f (pix)	1.00	−0.01	−0.05	−0.06	−0.03	−0.09	0.03	0.01	−0.04	−0.03	0.03
X_p (pix)		1.00	0.04	−0.04	−0.23	−0.03	0.02	−0.03	0.03	0.20	−0.02
Y_p (pix)			1.00	0.18	−0.17	−0.01	−0.00	0.00	−0.00	0.03	0.43
b_1				1.00	−0.00	0.03	−0.02	0.02	−0.02	0.12	0.01
b_2					1.00	−0.00	0.00	−0.00	0.00	−0.03	−0.19
k_1						1.00	**−0.96**	**0.91**	**−0.86**	−0.07	0.02
k_2							1.00	**−0.99**	**0.95**	0.08	−0.01
k_3								1.00	**−0.99**	−0.08	0.01
k_4									1.00	0.08	−0.01
p_1										1.00	0.17
p_2											1.00

TABLE A7 Correlation matrix of Inspire 2/X4s camera i.O. parameters in CG flight mode (parameters are described in the caption to Table A3)

	f (pix)	X_p (pix)	Y_p (pix)	b_1	b_2	k_1	k_2	k_3	k_4	p_1	p_2
f (pix)	1.00	−0.17	−0.36	−0.08	−0.06	−0.09	0.02	0.02	−0.05	0.03	0.03
X_p (pix)		1.00	0.14	−0.07	0.25	−0.04	0.06	−0.07	0.07	0.53	0.19
Y_p (pix)			1.00	−0.23	0.02	−0.01	0.04	−0.06	0.07	0.05	0.36
b_1				1.00	0.00	0.04	−0.04	0.03	−0.03	−0.01	−0.04
b_2					1.00	−0.03	0.03	−0.03	0.03	−0.01	−0.06
k_1						1.00	**−0.96**	**0.91**	**−0.86**	−0.10	−0.08
k_2							1.00	**−0.99**	**0.95**	0.11	0.08
k_3								1.00	**−0.99**	−0.13	−0.09
k_4									1.00	0.14	0.10
p_1										1.00	0.58
p_2											1.00

TABLE A8 Correlation matrix of Inspire 2/X4s camera i.O. parameters in CGC flight mode (parameters are described in the caption to Table A3)

	f (pix)	X_p (pix)	Y_p (pix)	b_1	b_2	k_1	k_2	k_3	k_4	p_1	p_2
f (pix)	1.00	−0.06	−0.55	−0.26	−0.06	−0.36	0.32	−0.28	0.25	0.01	−0.04
X_p (pix)		1.00	0.11	−0.00	0.30	−0.03	0.03	−0.03	0.03	0.65	0.21
Y_p (pix)			1.00	−0.26	0.08	−0.05	0.04	−0.05	0.05	0.08	0.39
b_1				1.00	−0.02	0.06	−0.05	0.05	−0.04	−0.02	−0.03
b_2					1.00	−0.00	0.00	0.00	−0.00	0.03	−0.00
k_1						1.00	**−0.97**	**0.92**	**−0.87**	−0.09	−0.09
k_2							1.00	**−0.99**	**0.96**	0.10	0.09
k_3								1.00	**−0.99**	−0.12	−0.10
k_4									1.00	0.13	0.11
p_1										1.00	0.52
p_2											1.00

TABLE A9 Correlation matrix of Phantom 4 Pro+ camera i.O. parameters in PA flight mode (parameters are described in the caption to Table A3)

	f (pix)	X_p (pix)	Y_p (pix)	b_1	b_2	k_1	k_2	k_3	k_4	p_1	p_2
f (pix)	1.00	−0.11	0.05	−0.04	−0.02	−0.06	−0.00	0.02	−0.03	0.04	−0.05
X_p (pix)		1.00	0.02	0.70	−0.16	−0.01	0.02	−0.03	0.03	0.39	0.12
Y_p (pix)			1.00	0.19	0.62	−0.02	0.01	−0.01	0.01	0.02	0.25
b_1				1.00	−0.00	0.00	−0.01	0.01	−0.01	0.25	0.08
b_2					1.00	−0.01	0.01	−0.01	0.01	−0.04	−0.09
k_1						1.00	**−0.97**	**0.93**	**−0.89**	−0.01	−0.00
k_2							1.00	**−0.99**	**0.96**	0.00	0.02
k_3								1.00	**−0.99**	−0.00	−0.02
k_4									1.00	0.00	0.01
p_1										1.00	0.01
p_2											1.00

TABLE A10 Correlation matrix of Phantom 4 Pro+ camera i.O. parameters in CG flight mode (parameters are described in the caption to Table A3)

	f (pix)	X_p (pix)	Y_p (pix)	b_1	b_2	k_1	k_2	k_3	k_4	p_1	p_2
f (pix)	1.00	0.00	0.46	−0.03	0.02	−0.05	−0.00	0.02	−0.04	0.06	−0.00
X_p (pix)		1.00	−0.07	0.36	−0.24	−0.01	0.00	−0.00	0.00	0.59	−0.01
Y_p (pix)			1.00	0.09	0.40	0.00	−0.03	0.03	−0.04	0.07	0.54
b_1				1.00	−0.01	0.06	−0.08	0.08	−0.07	0.12	−0.15
b_2					1.00	−0.00	−0.00	−0.00	−0.00	0.12	0.17
k_1						1.00	**−0.97**	**0.92**	**−0.88**	−0.01	0.00
k_2							1.00	**−0.99**	**0.96**	0.00	0.01
k_3								1.00	**−0.99**	−0.00	−0.01
k_4									1.00	0.01	0.01
p_1										1.00	0.05
p_2											1.00

TABLE A11 Correlation matrix of Phantom 4 Pro+ camera i.O. parameters in CGC flight mode (parameters are described in the caption to Table A3)

	f (pix)	X_p (pix)	Y_p (pix)	b_1	b_2	k_1	k_2	k_3	k_4	p_1	p_2
f (pix)	1.00	−0.13	−0.68	−0.44	−0.24	−0.36	0.33	−0.30	0.27	−0.05	−0.10
X_p (pix)		1.00	0.12	0.26	0.17	−0.00	0.00	−0.00	0.01	0.68	0.14
Y_p (pix)			1.00	0.18	0.31	−0.03	0.01	−0.01	0.00	0.08	0.48
b_1				1.00	0.12	0.04	−0.06	0.06	−0.06	0.13	−0.01
b_2					1.00	−0.01	0.00	0.00	−0.00	0.02	0.13
k_1						1.00	**−0.97**	**0.92**	**−0.87**	0.01	−0.02
k_2							1.00	**−0.99**	**0.96**	0.00	0.01
k_3								1.00	**−0.99**	−0.02	−0.01
k_4									1.00	0.04	0.02
p_1										1.00	0.37
p_2											1.00

TABLE A12 Correlation matrix of Mavic Pro camera i.O. parameters in PA flight mode (parameters are described in the caption to Table A3)

	f (pix)	X_p (pix)	Y_p (pix)	b_1	b_2	k_1	k_2	k_3	k_4	p_1	p_2
f (pix)	1.00	−0.11	0.01	−0.05	−0.07	−0.03	−0.06	0.12	−0.17	0.03	−0.04
X_p (pix)		1.00	−0.00	0.67	−0.17	0.10	−0.11	0.13	−0.14	0.44	0.04
Y_p (pix)			1.00	0.13	0.58	0.05	−0.08	0.10	−0.13	0.06	0.32
b_1				1.00	−0.00	0.08	−0.11	0.12	−0.14	0.25	−0.03
b_2					1.00	0.01	−0.02	0.02	−0.03	−0.04	−0.05
k_1						1.00	**−0.97**	**0.92**	**−0.87**	0.05	0.04
k_2							1.00	**−0.99**	**0.96**	−0.09	−0.04
k_3								1.00	**−0.99**	0.10	0.05
k_4									1.00	−0.12	−0.06
p_1										1.00	0.02
p_2											1.00

TABLE A13 Correlation matrix of Mavic Pro camera i.O. parameters in CG flight mode (parameters are described in the caption to Table A3)

	f (pix)	X_p (pix)	Y_p (pix)	b_1	b_2	k_1	k_2	k_3	k_4	p_1	p_2
f (pix)	1.00	−0.00	0.06	−0.09	−0.07	0.03	−0.16	0.26	−0.35	0.01	0.03
X_p (pix)		1.00	−0.10	0.37	0.02	0.01	−0.02	0.02	−0.02	0.53	−0.05
Y_p (pix)			1.00	−0.12	0.30	−0.01	0.00	−0.00	−0.00	−0.05	0.50
b_1				1.00	−0.01	0.06	−0.05	0.04	−0.03	0.04	−0.21
b_2					1.00	0.00	0.01	−0.02	0.02	0.09	0.03
k_1						1.00	**−0.97**	**0.91**	**−0.85**	0.02	−0.01
k_2							1.00	**−0.98**	**0.95**	−0.03	0.01
k_3								1.00	**−0.99**	0.03	−0.01
k_4									1.00	−0.03	0.00
p_1										1.00	0.01
p_2											1.00

TABLE A14 Correlation matrix of Mavic Pro camera i.O. parameters in CGC flight mode (parameters are described in the caption to Table A3)

	f (pix)	X_p (pix)	Y_p (pix)	b_1	b_2	k_1	k_2	k_3	k_4	p_1	p_2
f (pix)	1.00	−0.11	−0.82	−0.26	−0.24	−0.10	−0.01	0.09	−0.16	−0.02	−0.15
X_p (pix)		1.00	0.09	0.16	0.34	−0.04	0.04	−0.05	0.05	0.78	0.04
Y_p (pix)			1.00	−0.11	0.27	−0.10	0.17	−0.24	0.29	0.00	0.39
b_1				1.00	0.08	0.02	−0.01	−0.00	0.01	0.05	−0.10
b_2					1.00	−0.04	0.06	−0.08	0.10	−0.04	−0.08
k_1						1.00	**−0.97**	**0.92**	**−0.86**	−0.02	−0.03
k_2							1.00	**−0.99**	**0.95**	0.02	0.04
k_3								1.00	**−0.99**	−0.02	−0.07
k_4									1.00	0.01	0.09
p_1										1.00	0.05
p_2											1.00